DEVELOPMENT AND CHARACTERIZATION OF TUNGSTATES AND MOLYBDATES FOR LI-ION BATTERIES

A THESIS SUBMITTED TO
THE GRADUATE SCHOOL OF NATURAL AND APPLIED SCIENCES
OF
MIDDLE EAST TECHNICAL UNIVERSITY

By

BURÇİN KAYGUSUZ

IN PARTIAL FULFILLMENT OF THE REQUIREMENTS
FOR
THE DEGREE OF MASTER OF SCIENCE
IN
METALLURGICAL AND MATERIALS ENGINEERING

SEPTEMBER 2016

Approval of the thesis:

DEVELOPMENT AND CHARACTERIZATION OF TUNGSTATES AND MOLYBDATES FOR LI-ION BATTERIES

submitted by **BURÇİN KAYGUSUZ** in partial fulfilment of the requirements for the degree of **Master of Science in Metallurgical and Materials Engineering Department, Middle East Technical University** by,

Prof. Dr. Gülbin Dural Ünver
Dean, Graduate School of **Natural and Applied Sciences** _____

Prof. Dr. C. Hakan Gür
Head of Department, **Metallurgical and Materials Engineering** _____

Prof. Dr. M. Kadri Aydınol
Supervisor, **Metallurgical and Materials Eng. Dept., METU** _____

Examining Committee Members:

Prof. Dr. Mehmet Parlak
Physics Dept., METU _____

Prof. Dr. Mehmet Kadri Aydınol
Metallurgical and Materials Eng. Dept., METU _____

Assoc. Prof. Dr. Z. Göknur Cambaz Büke
Material Science and Nanotechnology Eng. Dept., TOBB-ETU _____

Assist. Prof. Dr. Mert Efe
Metallurgical and Materials Eng. Dept., METU _____

Assist. Prof. Dr. Metehan Erdoğan
Materials Eng. Dept., Yıldırım Beyazıt University _____

Date: 08.09.2016

I hereby declare that all information in this document has been obtained and presented in accordance with academic rules and ethical conduct. I also declare that, as required by these rules and conduct, I have fully cited and referenced all material and results that are not original to this work.

Name, Lastname: Burçin Kaygusuz

Signature:

ABSTRACT

DEVELOPMENT AND CHARACTERIZATION OF TUNGSTATES AND MOLYBDATES FOR LI-ION BATTERIES

Kaygusuz, Burçin

M. S., Department of Metallurgical and Materials Engineering
Supervisor: Prof. Dr. M. Kadri Aydınol

September 2016, 89 Pages

In recent years, the need for portable power, lithium ion batteries dominate the markets because of their advantages. Metal tungstates and molybdates (Metals: Fe, Ni, Co, Mn, Zn, Mg) are two important families of inorganic materials and have found many applications in various fields, such as catalysis, magnetic applications, humidity sensors, and photoluminescence. However, their use in energy storage applications is almost none. The tungstates and molybdates adapt monoclinic crystal structure and crystallize in P2/c and C2/m space group, respectively. Both structures have tunnels along certain crystal directions. Due to this unique crystal feature they are suitable for Li ion transport and intercalation, which has importance in Li-ion battery development. In this study, metal molybdates and tungstates were produced by sol-gel method. The structure of the obtained powders was investigated with X-Ray Diffraction and Scanning Electron Microscopy. These materials were used as active material against metallic lithium in a battery cell and the cells were characterized by using galvanostatic charge-discharge tests and electrochemical impedance spectroscopy. According to results, metal tungstates and molybdates have

high capacity for few cycles and then capacity loss was observed. It needs further intensive investigation to understand the lithium insertion mechanisms underlying, so as to improve cycle life to make it a commercially available material.

Keywords**:** Li-ion Batteries, tungstates, molybdates, sol-gel, electrochemical tests

ÖZ

LİTYUM İYON BATARYALAR İÇİN TUNGSTAT VE MOLİBDATLARIN GELİŞTİRİLMESİ VE KARAKTERİZASYONU

Kaygusuz, Burçin

Yüksek Lisans, Metalurji ve Malzeme Mühendisliği Bölümü
Tez Yöneticisi: Prof. Dr. M. Kadri Aydınol

Eylül 2016, 89 Sayfa

Lityum iyon bataryalar, sahip olduğu avantajlardan ötürü son yıllarda taşınabilir güç uygulamalarında yaygın olarak kullanılır hale gelmiştir. Metal tungstatlar ve molibdatlar inorganik malzemelerin iki önemli ailesini oluştururlar ve katalizör olarak, manyetik uygulamalarda, nem sensörü olarak ya da fotolüminesans uygulamaları gibi bir çok alanda kullanılmaktadırlar. Fakat enerji için uygulamaları neredeyse yok gibidir. Tungstatlar ve molibdatlar monoklinik kristal yapısında ve sırasıyla P2/c ve C2/m uzay grubunda yer almaktadır. İki yapıda da belirli kristal doğrultusunda tüneller yer almaktadır. Bu eşsiz kristal yapı sayesinde bu bileşikler lityum iyonu taşınımı ve interkalasyonu için uygundur ve bu özellik lityum iyon bataryalarının gelişimi için çok önemlidir. Bu çalışmada metal tungstatlar ve molibdatlar sol-jel metoduyla üretilmiştir. Elde edilen tozların yapısı X-Işını Kırınım ve Taramalı Elektron Mikroskobu ile incelenmiştir. Bu maddeler bir batarya hücresi içerisinde metalik lityuma karşı aktif madde olarak kullanılmış ve hücreler

galvanostatik şarj-deşarj testleri ve elektrokimyasal empedans spektroskopisi kullanılarak karakterize edilmiştir. Elde edilen sonuçlara göre bileşikler, ilk çevrimlerde yüksek kapasite göstermişlerdir sonrasında ise kapasite kaybı yaşamışlardır. Malzemelerin çevrim ömrünü artırmak açısından, bileşiklerin içindeki lityum iyon yayınımını ve faz dönüşümlerini daha detaylı bir şekilde araştırmanın gerekliliği ortaya çıkmıştır.

Anahtar kelimeler: Lityum-iyon bataryalar, tungstatlar, molibdatlar, sol-jel, elektrokimyasal testler

Dedicated to my family

ACKNOWLEDGEMENTS

This thesis would be not possible without the support of many people in my life. It was quite an enjoyable and memorable experience that I worked with nice and intelligent people. Thus, I take this chance to acknowledge each of them who have helped and supported me to this study.

I would like to express my gratitude to my supervisor, Prof. Dr. M. Kadri Aydınol for his guidance, advice, support, encouragement and valuable suggestions throughout the course of the studies.

Thanks are to all my laboratory team mates at the Department of Metallurgical and Materials Engineering, METU, especially, Burcu Miser, Berke Pişkin for their endless support in the completion of the thesis.

I also thank my wonderful best friends Yadigar Seymen, H. Gözde Yıldırım, Cansu Yağlıkçı and Esra Soy and all my great friends for their friendship, support, encouragement and motivation throughout my undergraduate and graduate studies.

Finally, I would like to thank my all family members especially my elder brothers Yasin and Yalçın for their endless support, encouragement, motivation, and advices. Without my family, this master thesis would not have been possible.

This study was supported by The Scientific and Technological Research Council of Turkey (Tübitak) with MS work Scholarship (2210-C).

TABLE OF CONTENTS

ABSTRACT.....v

ÖZ.....vi

ACKNOWLEDGEMENTS.....vii

TABLE OF CONTENTS.....ix

LIST OF TABLES.....xi

LIST OF FIGURES.....xiii

CHAPTERS

1.INTRODUCTION.....1

2.LITERATURE REVIEW.....3

2.1. Batteries.....3

2.1.1.History of batteries.....3

2.1.2. Components of batteries.....5

2.2.Lithium Ion Batteries.....6

2.2.1. History of Lithium-Ion Batteries.....6

2.2.2. Construction of Li-ion Battery.....7

2.2.3. Component of Lithium-ion Batteries.....10

a. Electrolyte.....10

b. Electrodes.....12

b.a. Cathode materials of Lithium-ion batteries.....15

b.b. Anode Materials of lithium-ion batteries.....17

c. Others.....18

2.3.Materials.....19

2.3.1. Cadmium tungstate ($CdWO_4$).....22

2.3.2. Cobalt tungstate ($CoWO_4$).....23

2.3.3. Iron tungstate ($FeWO_4$)..... 23
2.3.4. Magnesium tungstate ($MgWO_4$)..... 23
2.3.5. Manganese tungstate ($MnWO_4$)..... 24
2.3.6. Nickel tungstate ($NiWO_4$)..... 24
2.3.7. Zinc tungstate ($ZnWO_4$)..... 25
2.3.8. Cobalt molybdate ($CoMoO_4$)..... 25
2.3.9. Iron molybdate ($FeMoO_4$)..... 26
2.3.10. Magnesium molybdate ($MgMoO_4$)..... 26
2.3.11. Manganese molybdate ($MnMoO_4$)..... 26
2.3.12. Nickel molybdate ($NiMoO_4$)..... 27
3.EXPERIMENTAL..... 29
3.1.Powder synthesis via Sol-gel..... 30
3.2. Cell making..... 34
3.2.1. Carbon coating of powders..... 34
3.2.2. Preparing the electrode..... 34
3.2.3. Cell assembly..... 35
3.3. Electrochemical Testing..... 35
3.4.Material Characterization..... 37
4.RESULTS AND DISCUSSION..... 39
4.1. Production of Materials Results..... 39
4.1.1. Production of $CdWO_4$..... 39
4.1.2. Production of $CoWO_4$..... 42
4.1.3. Production of $FeWO_4$..... 44
4.1.4. Production of $MgWO_4$..... 47
4.1.5. Production of $MnWO_4$..... 49
4.1.6. Production of $NiWO_4$..... 51
4.1.7. Production of $ZnWO_4$..... 52
4.1.8. Production of $CoMoO_4$..... 54
4.1.9. Production of FeMoO4..... 58
4.1.10. Production of $MgMoO_4$..... 60
4.1.11. Production of $MnMoO_4$..... 62
4.1.12. Production of $NiMoO_4$..... 63
4.2. Results of carbon coating of powders..... 64
4.3. Electrochemical Tests Results..... 70

4.3.1.Galvanostatic Charge-Discharge tests.....71
4.3.2.Electrochemical Impedance Spectroscopy.....81
5.CONCLUSION.....83
REFERENCES.....85

LIST OF TABLES

Tables

Table 2.1. Act of electrodes during charge and discharge..... 12

Table 2.2. Properties of some common type anode material.....18

Table 2.3. Space group of materials in this study.....23

Table 4.1. Different calcination temperatures, duration and produced material compositions.....40

Table 4.2. Comparison of lattice parameters of $CdWO_4$ 42

Table 4.3. Comparison of lattice parameters of $CoWO_4$ 44

Table 4.4. Experimental parameters to produce $FeWO_4$ 45

Table 4.5. Comparison of lattice parameters of $FeWO_4$.....47

Table 4.6. Comparison of lattice parameters of $MgWO_4$.....48

Table 4.7. Comparison of lattice parameters of $MnWO_4$.....50

Table 4.8. Comparision of lattice parameters of $NiWO_4$.....52

Table 4.9. Comparison of lattice parameters of $ZnWO_4$.....54

Table 4.10. Production parameters and composition of produced material.....55

Table 4.11. Lattice parameters of different $CoMoO_4$ phases at different production parameters.....57

Table 4.12. Comparison of lattice parameters of $MgMoO_4$.....61

Table 4.13. Comparison of lattice parameters of $MnMoO_4$.....63

Table 4.14. Comparison of lattice parameters of $NiMoO_4$.....64

Table 4.15. Capacity retention of molybdates during cycling. Values were given in percentage with respect to the initial discharge capacity.....73

Table 4.16**.** Capacity retention of tungstates during cycling. Values were given in percentage with respect to the initial discharge capacity.....73

Table 4.17. Number of lithium atoms inserted in molybdates at the initial, fifth and final cycles.....74

Table 4.18. Number of lithium atoms inserted in tungstates at the initial, fifth and final cycles.....74

Table 4.19. Determined lattice parameters and unit cell volume of pristine and lithiated $MgWO_4$.....77

Table 4.20. Charge transfer resistance of molybdates and tungstates in ohm.....81

LIST OF FIGURES

Figures

Figure 2.1. Volta pile……...……...4

Figure 2.1. (a) Schematic of Plante‘s lead-acid cell; (b) early illustration of a battery of nine *Plante cells*……..…….....4

Figure 2.3. Interior structure of Li-ion battery.....6

Figure 2.4. Cross-sectional view of a cylindrical and prismatic Li-ion cell 8

Figure 2.5. Example of a piles prismatic cell, (2) a cylindrical lithium-ion cell in wound structure, (3) Examples of 18650 cylindrical cells (these are the most common consumer electronics lithium-ion cell form factor), (4) Cell being unwound revealing multiple layers, (5) Example of a hard cover prismatic cell, (6) Example of a softpouch polymer cell.....9

Figure 2.6. Schematic representation of various Li-ion battery configurations. **a**, Cylindrical; **b**, coin; **c**, prismatic; and **d**, thin and flat.....10

Figure 2.7. Lithium-ion cell operation 13

Figure 2.8. Crystal structure of the three lithium-insertion compounds.....14

Figure 2.9. (a)The schematic representation of the crystal structure of $LiMPO_4$ and (b) $LiFePO_4$ 16

Figure 2.10. Comparision of Wolframite structure (left) and scheelite structure (right). Small full circles: A cations at 1/2, small open circles: Mo or W cations at 0, large open circles: oxygens at +1/4 and large full circles: oxygens at -1/4 20

Figure 2.11. Crystal structure of space group 12 (left; $MnMoO_4$) and space group 13 (right ; $MnWO_4$) 21

Figure 3.1. Main steps of experimental procedure.....29

Figure 3.2. Scheme of the sol-gel process.....31

Figure 3.3. Schematic representation of powder production steps.....32

Figure 3.4. Schematic representation of making the electrodes.....34

Figure 3.5. The equivalent circuit for surface film model.....36

Figure 4.1. XRD pattern of $CdWO_4$ at 800 °C for 1 hour.....40

Figure 4.2. XRD pattern of $CdWO_4$ at 750 °C for 2 hours.....41

Figure 4.3. SEM images of $CdWO_4$ at 750°C for 2 hours.....41

Figure 4.4. XRD pattern of $CoWO_4$ at 800°C for 2 hours.....43

Figure 4.5. SEM images of $CoWO_4$ at 800°C for 2 hours.....43

Figure 4.6. XRD patterns of $FeWO_4$ at 800 °C, 2 hours at argon atmopshere (up) and air atmosphere (bottom) and iron (III) nitrate hexahydrate as iron source.....45

Figure 4.7. XRD pattern of $FeWO_4$ at 800 °C, 2 hours at air atmosphere, iron (II) sulphate heptahydrate as iron source.....46

Figure 4.8. SEM images of $FeWO_4$ at 800 °C for 2 hours at air atmosphere and sulphate source.....47

Figure 4.9. XRD pattern of $MgWO_4$ at 800 °C, 2 hours.....48

Figure 4.10. SEM images of $MgWO_4$ at 800 °C, 2 hours.....48

Figure 4.11. XRD pattern of MnO_4 at 800 °C, 2.5 hours.....49

Figure 4.12. SEM images of $MnWO_4$ at 800° C, 2.5 hours.....50

Figure 4.13. XRD pattern of $NiWO_4$ at 800 °C, 3 hours.....51

Figure 4.14. SEM images of $NiWO_4$ at 800 °C, 3 hours.....51

Figure 4.15. XRD spectrum for $ZnWO_4$ at 750 °C for 2, 4, 6 hours.....53

Figure 4.16. XRD pattern of $ZnWO_4$ at 750 °C, 2 hours.....53

Figure 4.17. SEM images of $ZnWO_4$ at 750°C, 2 hours.....54

Figure 4.18. XRD spectrum of $CoMoO_4$ at different temperatures and time.....55

Figure 4.19. SEM images of $CoMoO_4$ at 750 °C, 8 hours.....56

Figure 4.20. XRD spectrum of $FeMoO_4$ at 800 °C 2 and 4 hours.....58

Figure 4.21. XRD spectrum of $FeMoO_4$ at 800 °C 2 hours.....59

Figure 4.22. XRD spectrum of $FeMoO_4$ at 800 °C 4 hours.....59

Figure 4.23. XRD spectrum of $MgMoO_4$ at 750 °C, 2 and 4 hours.....60

Figure 4.24. XRD pattern of $MgMoO_4$ at 750 °C, 2 hours.....60

Figure 4.25. SEM images of $MgMoO_4$ at 750°C, 2 hours.....61

Figure 4.26. XRD pattern of $MnMoO_4$ at 800 °C, 2 hours.....62

Figure 4.27. SEM images of $MnMoO_4$ at 800 °C, 2 hours.....62

Figure 4.28. XRD pattern of $NiMoO_4$ at 800 °C, 2 hours.....63

Figure 4.29. SEM images of $NiMoO_4$ at 800 °C, 2 hours.....64

Figure 4.30 XRD pattern of carbon coated $CdWO_4$.....65

Figure 4.31. XRD patterns of carbon coated a)$CoMoO_4$, b)$CoWO_4$.....66

Figure 4.32. XRD pattern of carbon coated $FeWO_4$.....66

Figure 4.33. XRD patterns of carbon coated a)$MgMoO_4$, b)$MgWO_4$.....67

Figure 4.34. XRD patterns of carbon coated a)$MnMoO_4$, b)$MnWO_4$.....68

Figure 4.35. XRD patterns of carbon coated a)$NiMoO_4$, b)$NiWO_4$.....69

Figure 4.36. XRD patterns of carbon coated $ZnWO_4$, a) after ball mill and b) after heat treatment.....69

Figure 4.37. The Discharge Capacity graph of molybdates.....72

Figure 4.38. The Discharge Capacity graph of tungstates.....72

Figure 4.39. XRD spectrum of electrodes made by tungstates.....75

Figure 4.40. XRD spectrum of electrodes made by molybdates.....76

Figure 4.41. Crystal structure of $MgWO_4$, showing 2c and 2d Wyckoff positions with yellow and blue balls respectively. Grey, green and red balls represent Mg, W and O atoms respectively.....77

Figure 4.42. Voltage Profiles of molybdates.....79

Figure 4.43. Voltage Profiles of tungstates.....80

Figure 4.44. Nyquist impedance plots of materials at the discharged state.....82

CHAPTER 1

INTRODUCTION

The integration of two metals in an oxide structure may generate materials with chemical and physical properties that can cause to better performance in technology. The metal tungstates and molybdates are combined of transition metals such as Fe, Ni, Co, Mn etc. and tungsten or molybdenum. These materials are used for many applications but usage of energy applications is very limited. Both materials have tunnels along certain crystal directions in their structure. As a result of this combination, a crystal structure which is suitable for Li ion transport is formed. Li ion transportation and intercalation is important for Li-ion batteries development.

In this study, metal molybdates and tungstates were synthesized via sol-gel method. After processing of powders, all materials were characterized by using XRD and scanning electron microscopy (SEM).

Powder materials were coated by mechanically coating in a ball-mill with carbon black. Heat treatment was applied for stress relief and after which XRD method is used for the understanding of crystallinity of the structures.

Carbon coated materials were then used to make the electrodes. The active material, carbon black and binder were mixed in a certain ratio. After making the electrodes, the cells were installed within glove box filled with Argon gas. These materials were used as active material against metallic lithium in a battery cell, which were then characterized electrochemically.

CHAPTER 2

LITERATURE REVIEW

2.1. Batteries

Battery converts the chemical energy to electrical energy as a result of an oxidation-reduction reaction. When the electrochemical reactions occurred electrons are transferred from one material to another through an external circuit [1].

2.1.1. History of batteries

The first definition of electrochemical cell was defined by Alessandro Volta in 1880 (see Figure 2.1). The value of Volta's study is for understanding of cell chemistry and physics. However, in 1830 introduction of telegraph systems caused to developed reliable commercial batteries. In 1840, the first current galvanostatic battery was developed. In the 1870s, a more general consumer market for batteries was created by the manufacture of electric bell circuits for homes, offices and hotels [2].

The first efficient showing of a rechargeable cell was represented in 1859 by Gaston Plante. This cell consisted of two spirals lead sheet, separated by porous fabric and immersed in dilute sulfuric acid within a glass vessel (Figure 2.2a). This battery gave an output voltage of 2V. In March 1860, Plante presented a battery to the Academie Française in Paris; an illustration of these cells is shown in Figure 2.2b.

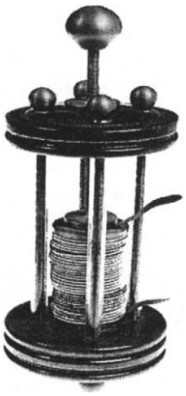


Figure 2.1. Volta pile [2].

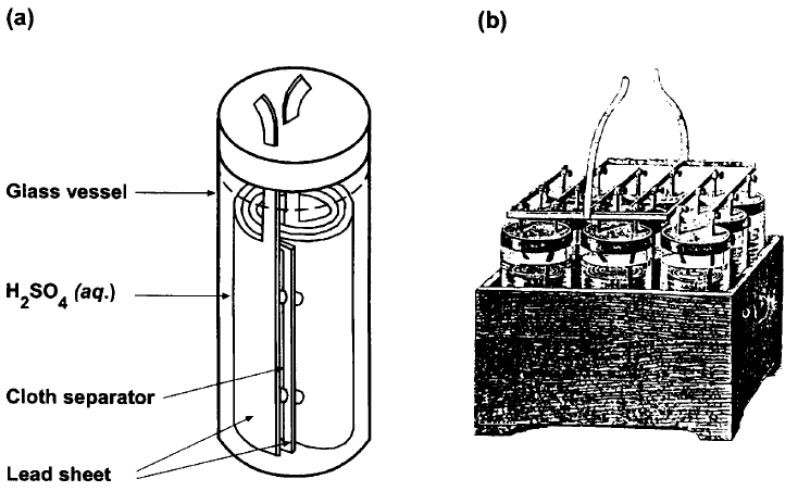


Figure 2.2. (a) Schematic of Plante‘s lead-acid cell; (b) early illustration of a battery of nine *Plante cells* [3].

The first work on batteries with alkaline solutions was reported in Sweden (1869-1924). Waldemar Jungner took out a patent for a ‘nickel cadmium battery’. Positive electrode is nickel hydroxide and, the negative electrode is a mixture of cadmium-iron powders. The electrodes were immersed in a concentrated solution of KOH.

Almost at the same time, Thomas Edison (1847-1931) developed and patented the 'nickel-iron battery'. This system was similar in principle, except negative electrode is iron rather than a cadmium-iron mixture. Both cells gave 1.2 V.

Battery science and technology have major advantages in the 20th century. Zinc as a primary battery has been improved. Totally new secondary batteries (nickel-metal hydrate, lithium-ion) have been also developed and commercialized. Finally, a number of secondary batteries are developed but not yet fully commercialized. Certainly, at the beginning of a new millennium, battery science and development is flourishing [3].

2.1.2. Components of batteries

Compound of battery can be meaned like cell. A battery contains one or more electrochemical cells. These cells can be constructed in series or in parallel or in other combination. The cell has three main units; anode, cathode and electrolyte. The oxidation reaction occurs during discharging at the anode and electrons move through the external circuit. The reduction reaction takes place at the cathode. There is another component which is electrolyte supplying ambience to complete electrical circuit for ion transportation among them the positive and negative electrodes [4]. The schematic of usual battery components are shown in Figure 2.3.

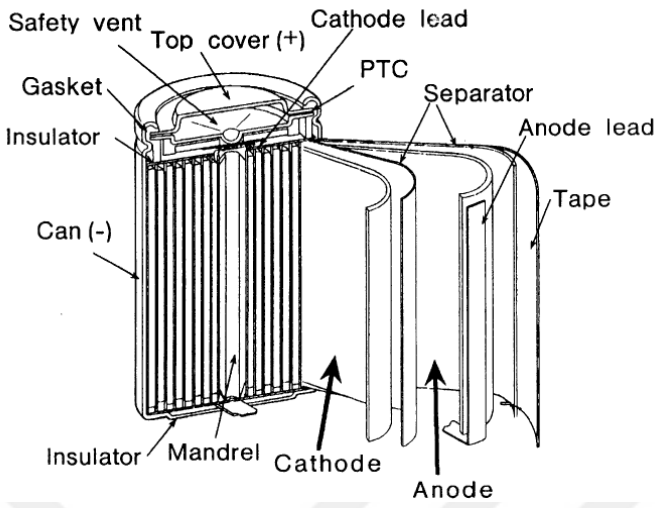


Figure 2.3. Interior structure of Li-ion battery [5]

2.2. Lithium Ion Batteries

2.2.1. History of Lithium-Ion Batteries

Lithium is the lightest element and supplies large energy density. For the development of new high-energy lithium battery systems total system should change based on new anodes, cathodes, and nonaqueous/ solid electrolytes.

As lithium metal formed a safety problem, lithium- intercalation material is used as an anode. In 1981, graphite is the first intercalation material and developed by H. Ikeda. After Ikeda, Goodenough filed his $LiCoO_2$ patent for an intercalation cathode material. In 1982, Basu found lithium interacalation into graphite in molten salt electrolytes at high temperature. Kuribayashi and Yoshino developed a new cell design carbon anode and a $LiCoO_2$ as cathode material. In 1992, Sony started to produce commercial cells which called Li-ion Battery [5].

Whereby Li-ion battery is commercialized by Sony, wide range of products is presented. One of them is gel-polymer Li-ion battery which is also referred to polymer Li-ion battery in the market. The microporous separator film is used by a layer of PVDF-HFP, or other polymer with liquid electrolyte and solid current collector foil in this battery [1].

2.2.2. Construction of Li-ion Battery

Generally, both prismatic and cylindrical Li-ion cells use the wound core structure. Active material amount, length, width and thickness are important properties for a better cell design and cell performance (see Figure 2.4) [6].

Mostly, wound type cells are designed for small cells, but prismatic configuration with flat plate construction is more common for large cell. Two cell types are designed for prismatic li-ion batteries: flat mandrel wound pseudo-prismatic and flat plate true prismatic cells [1].

Safety and maximum efficiency are major parameters for all researchers and designers while cell construction. Especially, form of electrodes and electrolytes are effective on these parameters.

Firstly, effect of electrodes is considered to design of battery, cell can be built by mass layers of (Fig. 2.5. (1)), or by winding long strips of electrodes for cylindrical cells (2 and 4), electrode piles or cylinders can be joined into hard cases that are sealed with gaskets (3), laser-welded hard cases (5), or enclosed in foil pouches with heat-sealed seams (5) [9].

Another issue which is effective on the construction of a cell is type of electrolyte. The liquid-electrolyte Li-ion battery technology has a great trading feat in the movable electronics market. Li-ion batteries are promptly needed to make small, thin and elastic tools. [9].

Tarascon et al. worked at practical plastic rechargeable lithium-ion batteries, they compared Bellcore's plastic lithium ion cell with liquid one in terms of cycle life, energy density and power. This plastic material combined of polymer structure, loaders, stabilizers etc. These components depend on aim of applications. They improved the first practical rechargeable lion battery, called plastic Li-ion (PLiON), which is different from general coin, cylindrical and prismatic type cell constructions (see Figure 2.6).

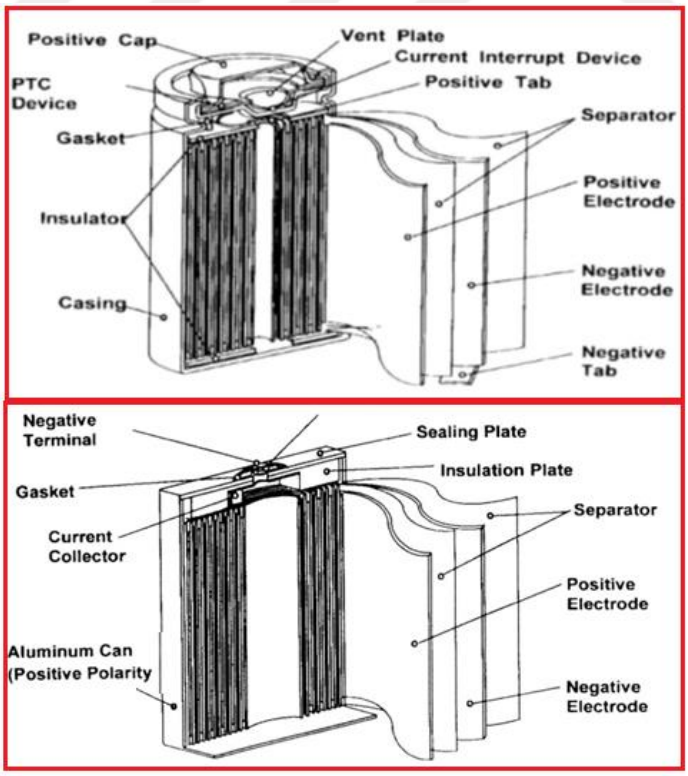


Figure 2.4. Cross-sectional view of a cylindrical and prismatic Li-ion cell [8].

The next generation of liquid electrolyte Li-ion cells were derived from the plastic Li-ion and are beginning to enter the market. This kind of battery is interesting because of the polymer ("plastic") laminated battery. It works definitely as liquid electrolyte Li-ion batteries, so lithium ions move through between the anode and the cathode. [5].



Figure 2.5. (1) Example of a piles prismatic cell, (2) a cylindrical lithium-ion cell in wound structure, (3) Examples of 18650 cylindrical cells (these are the most common consumer electronics lithium-ion cell form factor), (4) Cell being unwound revealing multiple layers, (5) Example of a hard cover prismatic cell, (6) Example of a softpouch polymer cell [8].

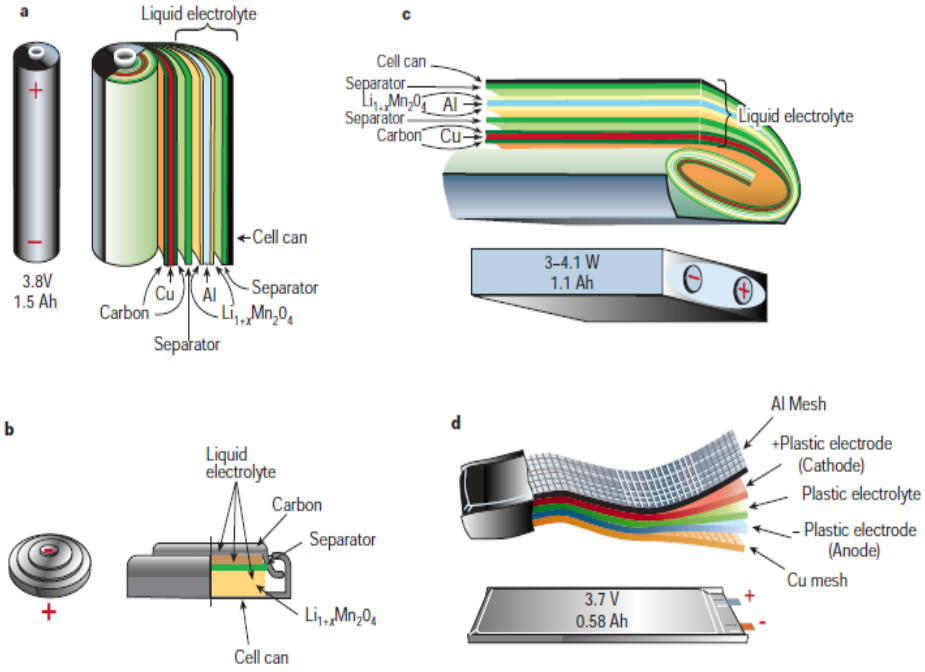


Figure 2.6. Schematic representation of various Li-ion battery configurations. **a**, Cylindrical; **b**, coin; **c**, prismatic; and **d**, thin and flat [5].

Additionally, coin cells are widely used for testing new battery materials especially to measure the charge-discharge capacities and performance in research laboratories [10].

2.2.3. Component of Lithium-ion Batteries

a. Electrolyte

A typical electrolyte for lithium-ion battery is a mixture of organic carbonates like ethylene carbonate or diethyl carbonate. The mixing ratio of carbonates depends on desired cell properties [8].

The electrolyte salts should have some properties:

1. *Ionic conductivity*
2. *Stability*
3. *SEI formation*

The most widely used lithium salts are; Lithium hexafluorophosphate ($LiPF_6$), lithium hexafluoroarsenate ($LiAsF_6$), lithium perchlorate ($LiClO_4$), lithium tetrafluoroborate ($LiBF_4$) **[**11].

In the literature, there are other type electrolytes such as organic /inorganic solid or liquid. Some researchers claim that the use of solid electrolytes eliminates the necessity of containment for liquid electrolyte which one simplifies the cell design as well as safety.

Jeffrey Fergus reviewed and compared ceramic and polymeric solid electrolytes for lithium-ion batteries. There are two general classes of materials used for solid electrolytes in lithium-ion batteries: inorganic ceramics and organic polymers. The most significant difference between these types is the mechanical properties. He focused on ionic conductivity of these types of electrolytes. Ionic conductivity of ceramic electrolytes is the result of movement of ionic point defects. When temperature increases, movement of ionic points will be fast and conductivity of electrolyte increases. Hence, ceramic solid electrolyte is more suitable for high temperature applications. Sulphides, oxides, and phosphates can be classified in ceramic electrolytes [12].

b. Electrodes

Oxidation, reduction, anode, cathode

To understand how electrodes work in lithium-ion batteries, some terms should be identified clearly. These are oxidation, reduction, anode, and cathode. *Oxidation* is loss of electrons, and in oxidation reducer is an electron donor. *Reduction* is gain of electrons, and in a reduction, oxidant is an electron acceptor.
A redox reaction can be usually written as:

$$aOxi + ne^- \leftrightarrow bRed$$

where *a*, *n* and *b* are balance coefficients [13].

Lithium ion batteries are known as "Rocking-chair" batteries due to movement of lithium ions move back and forth between the cathode and the anode. During discharge, cathode accepts electrons as positive electrode and vice versa anode donates electrons and oxidizes during discharge cycles. Table 2.1. show behaviour of electrodes in a rechargeable battery and Figure 2.7. show lithium-ion battery operation.

Table 2.1. Act of electrodes during charge and discharge [8].

Electrode type	Charge	Discharge
Positive electrode	Anode	Cathode
Negative electrode	Cathode	Anode

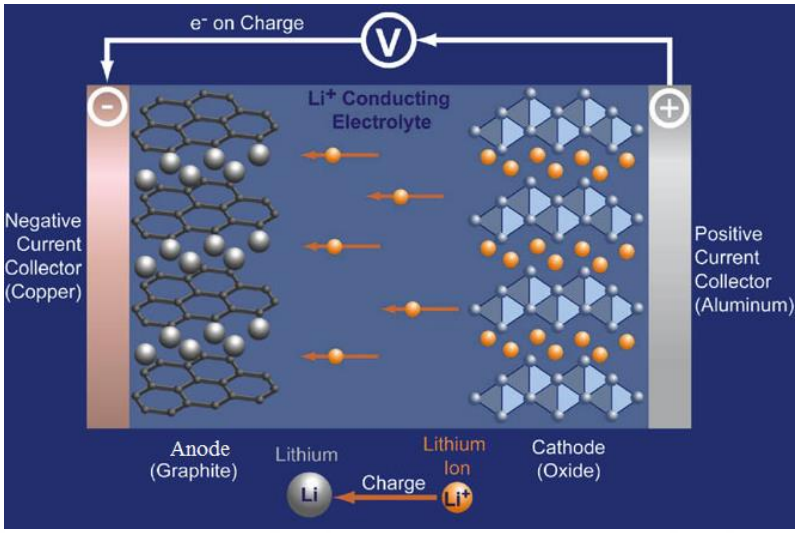


Figure 2.7. Lithium-ion cell operation [8].

The following reactions at the electrodes describe the operation of lithium - ion battery. Lithium ion move through the internal circuit (electrolyte) and electrons move through the external circuit as a result of these reactions.

Positive electrode:

$$[Li_{(1-x)}H_P] + xLi^+ + xe^- \underset{\text{charge}}{\overset{\text{discharge}}{\rightleftharpoons}} [LiH_P]$$

Negative electrode:

$$[LiH_N] \underset{\text{charge}}{\overset{\text{discharge}}{\rightleftharpoons}} [Li_{(1-x)}H_N] + xLi^+ + xe^-$$

Balace Equation:

$$[Li_{(1-x)}H_P] + [LiH_N] \underset{\text{charge}}{\overset{\text{discharge}}{\rightleftharpoons}} [LiH_P] + [Li_{(1-x)}H_N]$$ [13].

b.a. Cathode Material of Lithium-Ion Batteries

The most expensive part and key element of lithium-ion batteries is positive electrode which limits the performance of the batteries. In 1980, Goodenough was first developed $LiCoO_2$ and it is still used to be cathode material. The other milestone were made in 1986 for $LiMn_2O_4$ spinels and 1997 for the Li*M*PO_4 (*M* = Fe, Mn, *etc.*) olivine family. The crystal structures of some of cathode materials are shown in Figure 2.8. [14].

These materials have been used to be the electrode of commercial Lithium-ion batteries. Layered materials were preferred for high-energy systems, spinels and oxides were for high-power Li-ion batteries. But, all these lithium-insertion materials should have some special properties like good chemical stability, high rate capability, non-toxicity, low cost and safety [15, 16].

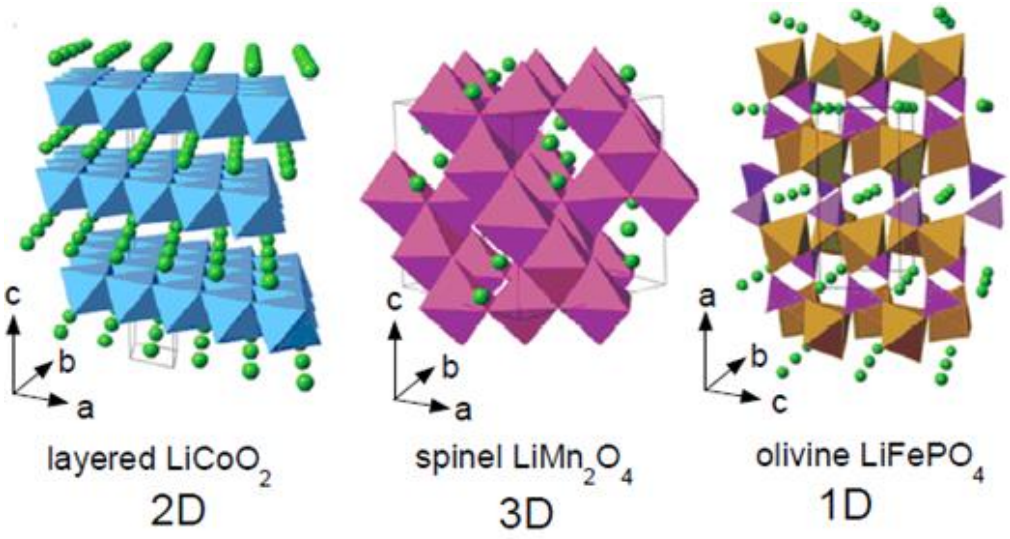


Figure 2.8. Crystal structure of the lithium-insertion compounds [14].

Selecting of cathode materials is important and some requirements of them are listed in followed;

1. The material reacts with lithium rapidly in a reversible reaction
2. It should be a good electronic conductor
3. The material should be stable,
4. The material should be cheap
5. The material should be environmentally friendly [18].

In the literature, four types of cathodes are studied in lithium batteries; Lithium manganese oxide (LMO), lithium cobalt oxide (LCO), nickel cobalt aluminium (NCA) and nickel manganese cobalt (NMC). LMO is generally used for HEV's, PHEV's and LCO was used for portable devices such as laptops, cell phones, but nowadays LMO is preferred instead of LCO because of cobalt metal prices increases and safety issues. NCA and NMC are developed for their high energy density [18].

Goodenough et al. developed $LiMPO_4$ (M = Fe, Mn, Ni, and Co) with an ordered olivine-type structure which has high theoretical specific capacity (~170 mAh g^{-1}). As shown in Figure 2.9, $LiMPO_4$ (M = Co, Fe, Mn, and Ni) adopts an olivine-related structure, and in LFP, Li^+ and Fe^{2+} fit octahedral sites, while P is located in tetrahedral sites in a lightly distorted hexagonal close-packed oxygen array. Although $LiFePO_4$ is the most attractive because of its high stability, low cost and high compatibility with environment, the main frailty of the $LiFePO_4$ are relatively poor potential and low electrical and ionic conductivity [16, 19].

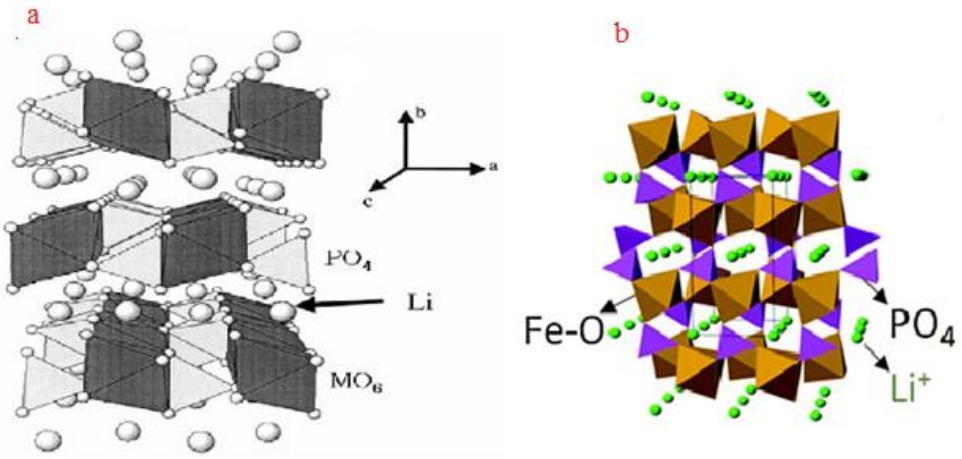


Figure 2.9. (a)The schematic representation of the crystal structure of $LiMPO_4$ and (b) $LiFePO_4$ [18].

b.b. Anode Materials of Lithium-Ion Batteries

Li metal was used as the anode material since the 1980s. However, new anode materials were required in li-ion batteries because Li metals forms dendrites and they case short circuit and also begin a thermal reaction on the cathode and cause fire. Additionally, Li metal suffers from poor cycle life [19].

The graphite anode for the Li-ion battery become available in trade for more than 20 years ago, and it is still used for anode material. Up to 1 Li atom per 6 C can be stored in the carbon layers. Carbon has some good properties; low cost, abundant availability, high Li diffusivity, and small volume change during lithiation/delithiation. Additionally, carbon-intercalation materials were studied as the anode for li-ion batteries because of safety problems of Li metal anode. For example, graphite, which has a layered structure, is able to intercalate Li ions and gives 372 mAh/g capacity. During the first cycles, electrolyte decomposes on the carbon surface and a passivation layer forms (SEI). All graphite surface is coated with SEI and further, electrolyte decomposition does not take place. Thus, the battery

can be cycled with no capacity loss. Graphitic anodes are used commercially in Li-ion batteries [19, 20].

Another anode material is lithium titanium oxide ($Li_4Ti_5O_{12}$ / LTO) which has good thermal stability, and high cycle life. A small voltage hysteresis is occurred as a result of small change. Also, LTO is very reliable because its high potential prevents Lithium dendrite formation, although it operates at high rates. [22, 23].

Recent studies show that Silicon (Si) is the most successful for anode due to its high gravimetric and volumetric capacity, low average delithiation potential, and chemical stability. Si has the highest known theoretical charge capacity (~4,200 mAh/g), which is more than 10 times that of actual graphite anodes (which have a capacity of ~372 mAh/g)

Wang et al. reported insertion and extraction of lithium ions in the Silicon anode cause very large volume change in the Si and $Li_{22}Si_5$ forms as a result of intercalation. This volume change cause stress cracking and loss of electrical contact [23].

From the literature, one can see that using of nanostructured silicon has several advantages over bulk silicon. Nano-silicon gives better result for stress tolerance and longer cycle life. Nanomaterials provide enhanced electrode surface area and shorter Li diffusion distances which enable faster charge/discharge rates. Additionally, it is known that nanomaterials have reduced energy barriers for alloy formation because of high surface to volume ratio [24].

Summary of some common type anode materials were shown in following Table 2.2.

Table 2.2. Properties of some common type anode materials [19].

Material	Lithiation voltage (V)	Delithiation voltage (V)	D (cm^2/sn)	Volume Change
Graphite	0.007-0.19	0.1-0.23	10^{-11}-10^{-7}	10%
LTO	1.55	1.58	10^{-12}-10^{-11}	0.2%
Si	0.05-0.2	0.31-0.47	10^{-13}-10^{-11}	270%
Sn	0.4-0.69	0.5-0.62	10^{-16}-10^{-13}	255%
Ge	0.2-0.5	0.5-0.7	10^{-12}-10^{-10}	240%

c. Others

The separator separates the cathode and anode in the batteries. It prevents the contact between two electrodes and also short circuit of the electrodes in the cells. Besides this, it plays an important role for safety in lithium-ion secondary batteries. On the other hand, it should not limit ionic transportation [25].

Separators are generally microporous which are made of either polymeric membrane or non-woven fabric material. Important criteria for their usage are chemical stability, mechanical strength, dimensional stability, wettability, porosity, permeability, thickness, thermal shrinkage, shut down and cost [26].

Usual materials used for separators include polyethylene (PE), polypropylene (PP), and their laminates. When temperature increases, a microporous film melts and fills the pores, and it stop the ion transport in the cell and prevent shutting down the battery. [27].

Another component of secondary batteries is current collectors. Current collector is used to transfer current throughout the cell to the active material. The most

widespread current collectors are thin foils of copper (for anode active materials) and aluminium (for cathode active materials) [8].

Copper is reliable for current collector of anode material especially at very low cell voltages. At high voltages aluminium is more suitable for being current collector. In some studies Al corrosion in electrolyte for lithium ion batteries are mentioned and the corrosion depends on mainly Li salts of the electrolyte [28].

2.3. Materials

Metal tungstates and molybdates are two important kinds of inorganic materials and they are used for many applications, such as catalysis, magnetic applications, humidity sensors, and photoluminescence. However studies related to their use in energy storage applications are very limited [28].

Most molybdates and tungstates crystallize either in the scheelite-type (tetragonal dipyramidal class) or in the wolframite-type (monoclinic) structure with the exception of $HgWO_4$ and $HgMoO_4$. While tungstates and molybdates of larger cations (r_A> 0.90 Å) crystallize in the scheelite structure where the molybdenum (or tungsten) atom accepts a tetrahedral coordination. Tungstates and molybdates with smaller bivalent cations (ionic radius < 0.77 Å) belong to the wolframite structure where the tungsten (or molybdenum) atom adopts an overall 6-fold coordination [29]. In addition, the high pressure phases of some molybdates are stable in the wolframite structure.

The scheelite structure can be defined as a cubic close packed arrangement of A^{2+} and BO_4^{2-} ions. All oxygen atoms are three-coordinated to cations in either scheelite or wolframite structures. In scheelite, oxygens are coordinated to two A and one B,

whereas half of the oxygens are coordinated to two B cations, other half of the oxygens are arranged to two A cations in the wolframite structure.

Another difference between scheelites and wolframites is the position of oxygen atoms. In the wolframite structure, the oxygens are hexagonally close-packed, however, the oxygens are not close packed and while B cation is in tetrahedral coordination to oxygen in the scheelite structure. Figure 2.10 illustrates the structures of wolframites and scheelites.

The tungstates and molybdates in the wolframite structure adapt monoclinic crystal structure and crystallize in P2/c (no.13) and C2/m (no.12) space group, respectively. On the other hand, scheelites adapt tetragonal crystal structure and crystallize in $I4_1/a$ (no.88) space group [30, 31, 32].

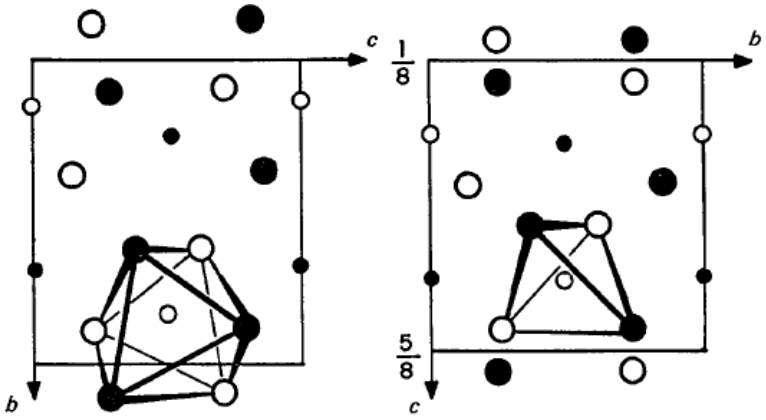


Figure 2.10. Comparison of Wolframite structure (left) and scheelite structure (right). Small full circles: A cations at 1/2, small open circles: Mo or W cations at 0, large open circles: oxygens at +1/4 and large full circles: oxygens at -1/4 [30].

The basic difference between space groups' no.12 and no.13 is the oxygen atom coordination of B (Mo or W) cation. In the monoclinic molybdate (no.12), Mo cation has tetrahedral oxygen coordination like the one in scheelite structure. In the monoclinic tungstate (no.13), however, W has octahedral oxygen coordination as in wolframite. Because of this feature, symmetry of the structures differs so as to give a base centred cell in no.12 and primitive cell in no.13. Furthermore, unlike scheelite structure, both structures (no.12 and no.13) have tunnels along *c* axis of the crystal structure, Figure 2.11. The tunnel diameters, for example for $MnWO_4$ and $MnMoO_4$ are approximately 2.77 Å and 2.67 Å respectively. This unique crystal feature offers a high diffusivity path for ion transport and space for intercalation. Such physical features are among important requirements in Li-ion battery development.

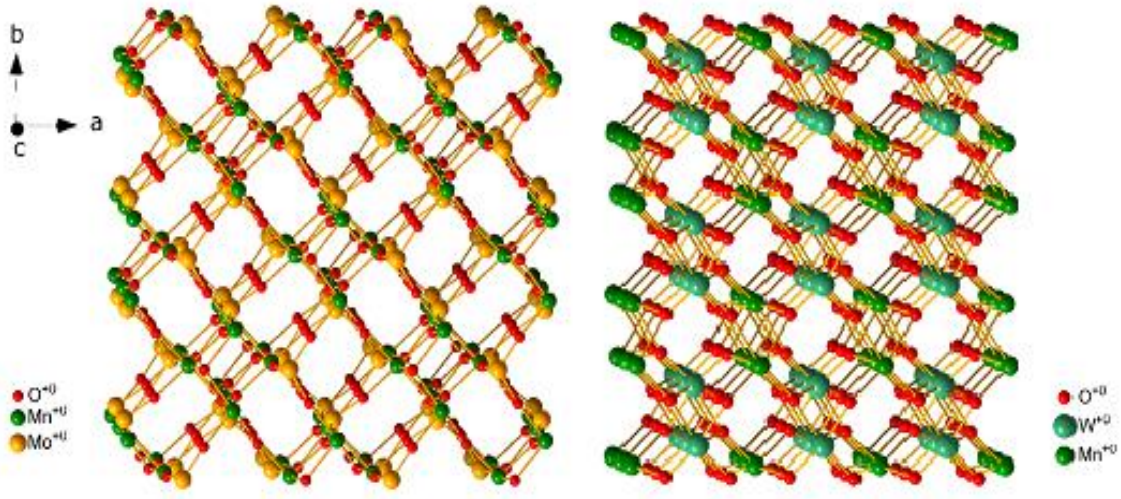


Figure 2.11. Crystal structure of space group no.12 (left; e.g. $MnMoO_4$) and space group no.13 (right; e.g. $MnWO_4$).

In this section, some properties, and applications of studied metal tungstates and molybdates are reviewed. The space groups of materials which were used in this study were given in Table 2.3.

Table 2.3. Space group of materials in this study.

P2/c (no.13)	**C2/m (no.12)**
$CdWO_4$	-
$CoWO_4$	$CoMoO_4$
$FeWO_4$	$FeMoO_4$
$MgWO_4$	$MgMoO_4$
$MnWO_4$	$MnMoO_4$
$NiWO_4$	$NiMoO_4$
$ZnWO_4$	-

2.3.1. Cadmium tungstate ($CdWO_4$)

Cadmium tungstate ($CdWO_4$) is an exciting material from a number of properties especially because of its optical, chemical, and structural properties. The lattice parameters of this material are a = 5.0289 Å, b = 5.8596 Å, c = 5.0715 Å and β = 91.519°. In this structure, each W is surrounded by 6 near O sites in approximately octahedral coordination [32, 33].

Cadmium tungstate is a luminescent material absorbs the energy of x-rays, γ-rays, and neutrons and then converts the energy to visible light. $CdWO_4$ has been widely used in high-energy radiation imaging and detection, spectrometry due to its high emission efficiency, high radiation stability, and high density [35].

2.3.2. Cobalt tungstate ($CoWO_4$)

$CoWO_4$ is in a monoclinic structure belonging to the P2/c space group, with unit cell parameters and a = 4.670 Å, b = 5.687 Å, c = 4.951 Å and β = 90.0° [35].

Cobalt tungstate ($CoWO_4$) is a well-known p-type semiconductor and used in many applications, such as pigment additives, oxygen carrier material for syngas production, microwave dielectric ceramics, and photovoltaic electrochemical cell [36].

2.3.3. Iron tungstate ($FeWO_4$)

Iron tungstate ($FeWO_4$) is crystallizing in a monoclinic structure belonging to the P2/c space group, with unit cell parameters a = 4.753 Å, b = 5.720 Å, c = 4.968 Å and β = 90.1°.

Iron tungstate has high potential in many technological applications such as scintillation detectors, optical fibres, laser hosts, humidity sensors, catalysts, pigments, etc. [35].

2.3.4. Magnesium tungstate ($MgWO_4$)

Magnesium tungstate has two polymorphs, α-$MgWO_4$ with a tricilinic structure at high temperature and β-$MgWO_4$ with a monoclinic structure that is stable at low temperature. Lattice parameters of β-$MgWO_4$ are a = 4.696 Å, b = 5.683 Å, c = 4.945 Å and β = 90.83°. $MgWO_4$ is also studied for optical, luminescence, and scintillation applications [37, 38].

2.3.5. Manganese tungstate ($MnWO_4$)

Manganese tungstate also known as the mineral hübnerite is a multiferroic material which combine magnetism and ferroelectricity.

The crystal structure is monoclinic and space group is the paramagnetic phase *P2/c* and the lattice parameters are a = 4.8237 Å, b = 5.7552 Å, c = 5.0019 Å and β = 91.0838° and consists of edge-sharing oxygen octahedral that make zig-zag chains along the *c* axis, with the Mn atoms located inside the distorted octahedra and the W atoms located between the chains [39, 40].

2.3.6. Nickel tungstate ($NiWO_4$)

Nickel tungstate crystallizes in the wolframite-like monoclinic P2/c structure. Hexagonal close-packed oxygen atoms and octahedral sites filled by Ni^{+2} and W^{+6} cations are in the structure. It has been studied as gas sensors, catalysts and electrochromic systems. [41, 42].

In only one work, Sagrariro and Fuentes studied electrochemical properties of lithium insertion in metal tungstates (MWO_4, M=Mn, Co, Ni and Cu) obtained by aqueous salt metathesis reactions. The electrochemical study showed that these compounds are not good hosts for insertion reactions because although they can incorporate a relatively large amount of lithium atoms (capacities above 1000 Ah/kg were obtained in some cases), the reaction is claimed to be irreversible [43].

2.3.7. Zinc tungstate ($ZnWO_4$)

Zinc tungstate is crystallizing in a monoclinic structure belonging to the P2/c space group, with unit cell parameters a = 4.6902 Å, b = 5.7159 Å, c = 4.9268 Å and β = 90.626° [44].

In the last studies, $ZnWO_4$ has attracted much affinity because of its catalytic properties and luminescent. Also, $ZnWO_4$ has been applied as a possible new material for microwave amplification by stimulated emission of radiation and optical hole burning lattice material, etc. [45].

2.3.8. Cobalt molybdate ($CoMoO_4$)

Cobalt molybdate ($CoMoO_4$) is one of the most important components of industrial catalysts for the partial oxidation of hydrocarbons. In addition, $CoMoO_4$ can also be applied in the electronics and bioscience industries due to its structural, magnetic, electronic and antibacterial properties [46].

Additionally, Kyung-Soo Park et al. studied $Ni_xCo_{1-x}MoO_4$ nanowire like anode material for lithium-ion batteries and x values were affected on the capacity. When x values are 0, 0.25 and 0.5, specific capacity was approximately 290 mAh/g after 20 cycles and x values are 0.75 and 1, the capacity changed to 520 mAh/g after 20 cycles. When the Ni content was increased, capacity of the Li-ion battery increased. [47].

In the literature, $CoMoO_4$ exists in several polymorphic forms. β-$CoMoO_4$ is a more stable form at low temperature. It has a monoclinic unit cell with parameters a = 9.67 Å, b = 8.85 Å, c = 7.76 Å and β = 113.88°. Above 650 K, β-$CoMoO_4$ transforms to α-$CoMoO_4$ characterised by a monoclinic unit cell (space group C2/m) and lattice parameter a = 10.21 Å, b = 9.26 Å and c = 7.02 Å and β = 106.938° [48].

2.3.9. Iron molybdate ($FeMoO_4$)

Iron molybdate is used for industrial application especially as a catalyst for oxidation of some alcohols and hydrocarbons, hydrogen storage and processing of heavy oils. Iron molybdate has two phases; α-$FeMoO_4$ at low temperature and β-$FeMoO_4$ at high temperature. Both phases are monoclinic with C2/m space group, however, the unit cell of β phase is 6% larger than other phase [49].

2.3.10. Magnesium molybdate ($MgMoO_4$)

Magnesium molybdates are studied for variety of applications such as scintillation material, microwave devices, catalysts, and optical devices. $MgMoO_4$ is especially a good detector target [50]. In addition, Yoon et al. reported the catalytic properties of magnesium molybdate in the oxidative dehydrogenation of alkanes [51]. $MgMoO_4$ has monoclinic structure (C2/m space group) and lattice parameters are a =10.273 Å, b = 9.288 Å, c =7.025 Å and β = 106.96° [52].

2.3.11. Manganese molybdate ($MnMoO_4$)

Manganese molybdate has interesting magnetic, catalytic and electrical properties. It is well known that $MnMoO_4$ has different polymorphs; α-$MnMoO_4$, β-$MnMoO_4$ and ω-$MnMoO_4$, where α-$MnMoO_4$ is the most dominant stable phase [53].

Sung-Soo Kim et al. reported that manganese molybdate is a negative electrode material for lithium secondary battery. High capacity (about 1800 Ah/kg) was obtained during the first lithiation [54]. In monoclinic structure the Mn atoms are octahedrally coordinated with oxygen while Mo atoms are tetrahedrally coordinated

with oxygen in C2/m space group. The lattice parameters are a = 10.4992 Å, b = 9.5304 Å, c = 7.1511 Å and β = 106.2° [53].

2.3.12. Nickel molybdate ($NiMoO_4$)

Nickel molybdate has attracted the interest of researchers because of their electronic and magnetic properties and their many applications, like photoluminescence and catalysis. Also, it has antiferromagnetic property below 19 K. It is monoclinic with C2/m space group [56].

CHAPTER 3

EXPERIMENTAL

To produce metal tungstate and molybdate materials, sol-gel method was used. After synthesis of powders, all materials were characterized by using XRD and scanning electron microscopy (SEM).

The synthesized powders needs a carbon coating process because a continuous carbon layer on the particles plays a significant role in electrical conductivity for all materials which have a conductivity problem. Powders were coated by mechanically coating in a ball-mill with carbon black. Heat treatment was applied for stress relief and after which XRD method is used for the understanding of crystallinity of the structures.

Carbon coated powder materials were then used to make the electrodes. The active material, carbon black and binder were mixed in a certain ratio. The suspension of all materials was stirred till therein is no agglomeration. The solution was coated on Cu foil by Doctor Blade. After making the electrodes, the cells were assembled in glove box filled with Argon. Finally, all cells for every material were tested by electrochemical methods such as galvanostatic charge-discharge tests and electrochemical impedance spectroscopy method. Schematic representation of experimental procedure was shown in Figure 3.1.

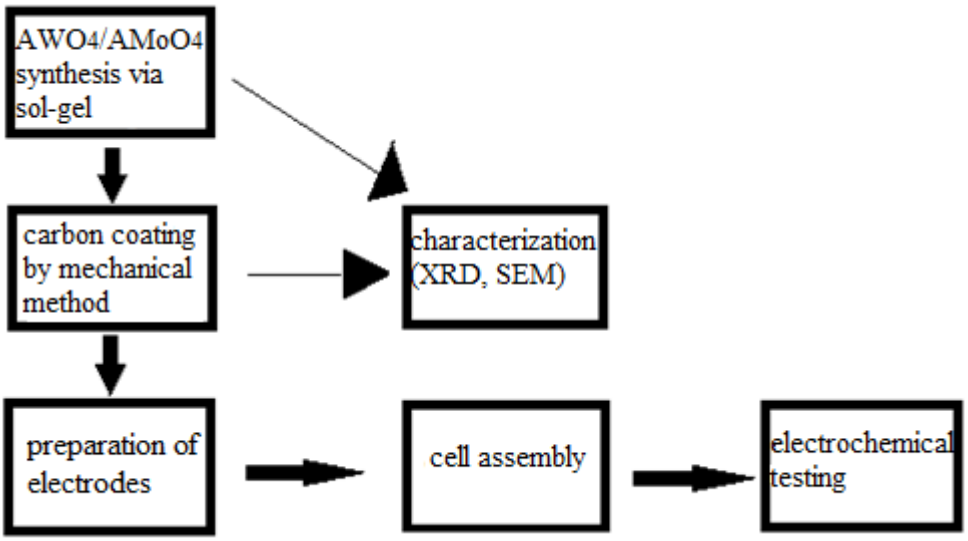


Figure 3.1. Main steps of experimental procedure.

3.1. Powder Synthesis via Sol-Gel

12 different ABO_4 type powder samples (A: Cd, Co, Fe, Mg, Mn, Ni, Zn and B: W/Mo) were produced by sol-gel method. These materials were $CdWO_4$, $CoWO_4$, $FeWO_4$, $MgWO_4$, $MnWO_4$, $NiWO_4$, $ZnWO_4$ and $CoMoO_4$, $FeMoO_4$, $MgMoO_4$, $MnMoO_4$, $NiMoO_4$ and all materials which were used in sol-gel and production process details were explained below.

The sol-gel method was used to produce of powder materials, since it is an easy and efficient way to synthesize the powder materials. The calcination temperatures and durations were studied according to phase diagrams and previous studies about the production of these materials.

To produce powder materials by sol-gel method the chemicals used are;

1. Ammonium tungstate oxide hydrate ($(NH_4)_6W_{12}O_{39.}5H_2O$)
2. Ammonium heptamolybdate tetrahydrate ($(NH_4)_6Mo_7O_{24}.4H_2O$)
3. Cadmium acetate dihydrate ($(CH_3COO)_2Cd.2H_2O$)
4. Cobalt(II) nitrate hexahydrate($Co(NO_3)_2.6H_2O$)
5. Iron(III) nitrate nonahydrate ($Fe(NO_3)_3.\ 9H_2O$)
6. Magnesium nitrate hexahydrate ($Mg(NO_3)_2.6H_2O$)
7. Manganese nitrate tetrahydrate ($MnN_2O_6.4H_2O$)
8. Nickel nitrate hexahydrate ($N_2NiO_6.\ 6H_2O$)
9. Zinc nitrate hexahydrate ($N_2O_6Zn.\ 6H_2O$)
10. Citric acid monohydrate ($C_6H_8O_7.H_2O$)
11. Ethylene glycol ($HOCH_2CH_2OH$).

To synthesis molybdates, 0.1 moles metal nitrate and 0.1 moles heptamolybdate tetrahydrate as Mo source were added into 150 ml distilled water. Then, citric acid (#of moles metal ions: citric acid= 1:1.1) and ethylene glycol (~0.01 moles) were added. This mixture was heated and stirred at around 170 °C. All chemicals were dissolved in distilled water and after about 2 hours, water was evaporated and “gel” was ready. Then this gel was dried at 100 °C for 24 hours in an oven. After drying, these precursors were put into a furnace at 350 °C for 1 hour for precalcination and then, they were calcinated at 750 – 850 °C for 2 – 6 hours.

To synthesis tungstates, 0.06 moles metal nitrate and 0.06 moles ammonium tungstate oxide hydrate as W source were added into 150 ml distilled water. Then, citric acid (#of moles metal ions: citric acid= 1:1.1) and ethylene glycol (~0.01 moles) were added. This mixture was heated and stirred at around 170 °C. All

chemicals were dissolved in distilled water and after about 2 hours, water was evaporated and “gel” was obtained. Then this gel was dried at 100 °C for 24 hours in an oven. After drying, these precursors were put into a furnace at 350 °C for 1 hour for precalcination and then, they were calcinated at 750 – 850 °C and 2 – 6 hours.

At the end of the process, approximately 15 grams of powder was obtained. Figures 3.2 and 3.3 shows another schematic representation of powder production by sol-gel.

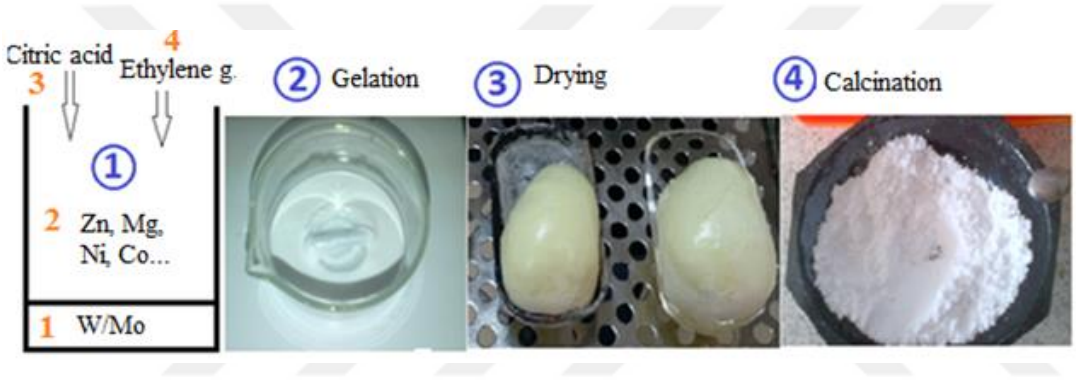


Figure 3.2. Schematic representation of powder production steps.

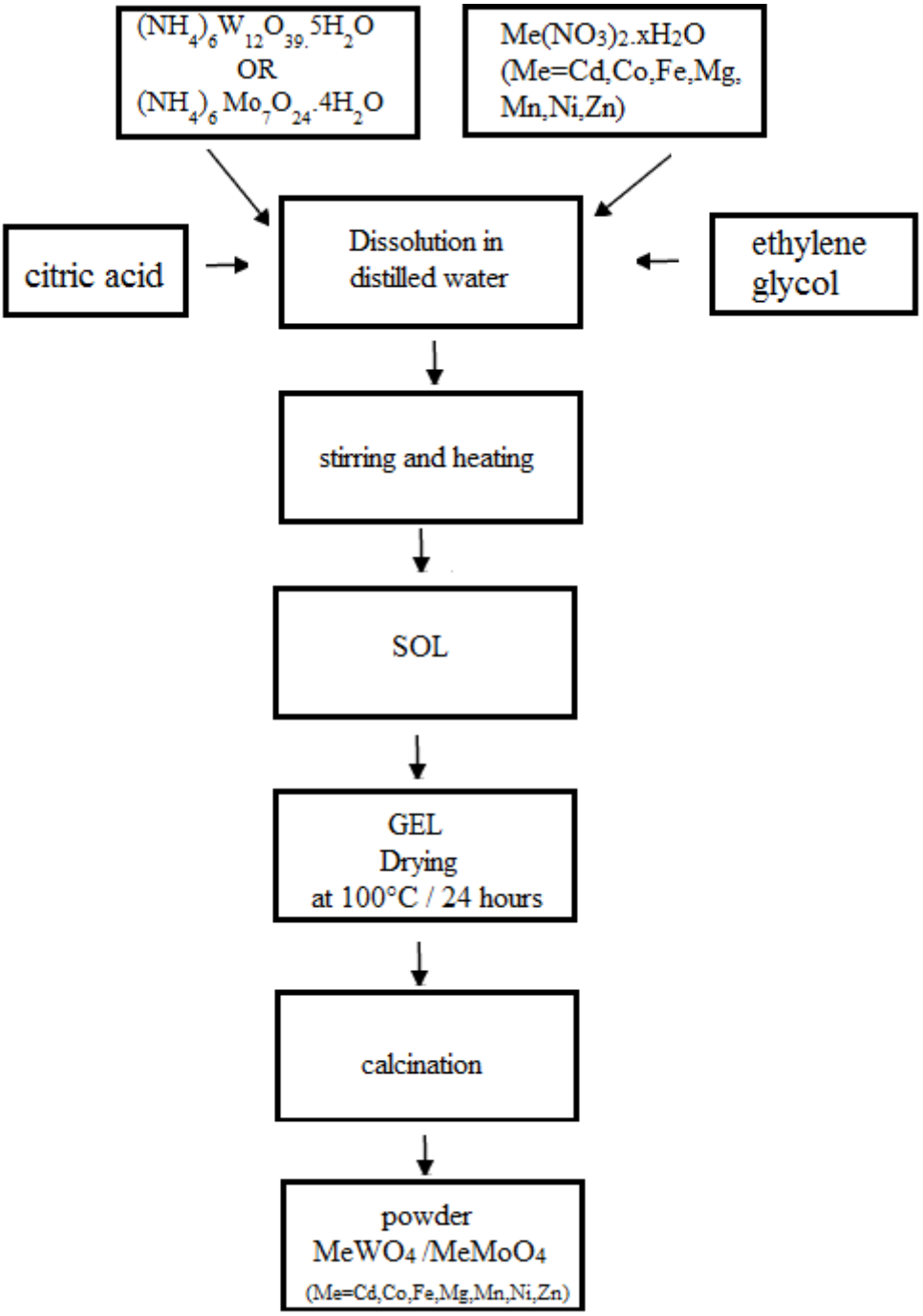


Figure 3.3. Scheme of the sol-gel process.

3.2. Cell making

3.2.1. Carbon coating of powders

The active powder material and Carbon black (Timcal Super C65) were weighted (material: carbon = 80:20) and then this mixture was put in a ball mill for 10 hours 200 rpm. Yttria-stabilized zirconia balls were used in ball-milling. Thus, powder material was coated with carbon by mechanical method. An additional heat treatment was applied to remove any residual stress that may have occurred during milling. It was leaved by keeping the samples at 650 °C for 4 h under Ar atmosphere.

3.2.2. Preparing the electrode

The active material, carbon black and binder were mixed in 90/5/5 weight ratio for making electrodes. Polyvinylidene difluoride (PVDF) binder was used as dissolved in N-methyl pyrrolidinone (NMP). The suspensions of all materials were put into ball mill for 10 minutes for better mixing. The solution was coated on Cu foil to obtain a 250 μm thick film. Doctor Blade method was used for coating. After coating, coated foil was dried for 2 h at 120 °C. The electrode was then pressed with 1 MPa pressure to support adhesion of partices and current collector Cu foil. Thickness of dry film on the electrode was approximately 100 μm. After pressing, the electrodes were cut into discs of 18 mm in diameter. Finally, they were further dried under vacuum at 120 °C overnight and transferred into glovebox. All steps till cell assembly were shown in following Figure 3.4.

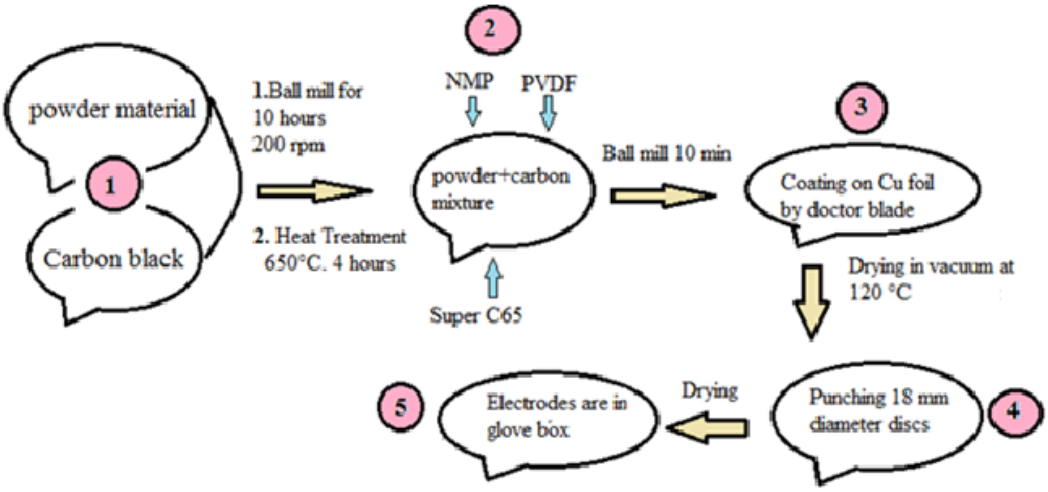


Figure 3.4. Schematic representation of making the electrodes.

3.2.3. Cell assembly

Cell making was carried out in a glove box filled with Ar. All produced electrodes were assembled into a two electrode cell using metallic lithium foil as counter electrode. A sheet of glass fiber was used as separator and electrolyte was 1M $LiPF_6$ in a 50:50 EC:DEC solution

3.3. Electrochemical Testing

a. Galvanostatic Charge-Discharge tests

The active materials were electrochemically characterized after cell assembly. The cells were charged and discharged with different rates on the Solartron 1480 multi-channel battery tester. A total of six galvanostatic charge/discharge cycles were applied using 0.5 mA, 1 mA and 1.5 mA (0.196 mA/cm^2, 0.393 mA/cm^2 and 0.598

mA/cm^2) current values. The cut-off voltage range in galvanostatic charge-discharge tests was 2.1 – 0.02 V vs. Li^+/Li.

b. Electrochemical Impedance Spectroscopy

EIS method is frequently used to analyse the performance of the batteries in terms of resistance. It also enables analysis and sorting of different types of faradaic and non-faradaic phenomena that incorporates resistive and capacitive loads in the cell. A typical impedance behaviour of lithium ion batteries involves two semi-circles in the Nyquist plot. The one at higher frequencies corresponds to capacitive and resistive loads due to SEI film formation. The second semi-circle at medium frequencies corresponds to double layer capacitance and charge transfer resistance. In order to determine the capacitance and resistance due to related phenomena, the experimental EIS data is fitted to an equivalent electric circuit made up of analogue circuit element.

The common circuit model used in lithium ion batteries is the surface film model, as shown in Figure 3.5. In this circuit Rel, Rf and Rct represent electrolyte resistance, surface film resistance and charge transfer resistance, respectively. The circuit elements indicated with Qf, Qdl and Qin are constant phase elements which represent the capacitive elements specific to surface film and double layer formation and lithium ion insertion into the bulk, respectively.

Electrochemical impedance measurements of the cells were carried out at the end of the final discharge operation using VersaSTAT3 electrochemical workstation at room temperature. The frequency range was from 300 kHz down to 3 mHz and the perturbation potential was ±10 mV with respect to open cell potential.

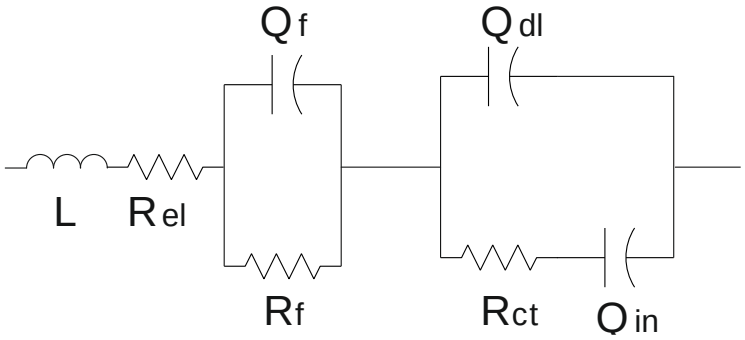


Figure 3.5. The equivalent circuit for surface film model.

3.2. Material Characterization

Crystal structure was analysed by using X-Ray Diffractometer (XRD, Bruker D8 Advance). Step scanning was 2 °/min and scans were run between 10° to 90°. Phase analysis and lattice parameters (*a*, *b*, *c* and *β*) of produced materials was determined by Rietveld Analysis by using MAUD software [56]. Atom positions and occupancies can also be determined by this software.

Structure data, which were obtained by previous experimental, were taken from Inorganic crystal structure database (ICSD).

ICSD numbers of materials are listed below:

ICSD no of $CdWO_4$:84454

ICSD no of $CoWO_4$:15851

ICSD no of $FeWO_4$:26811

ICSD no of $MgWO_4$:22357

ICSD no of $MnWO_4$:67907

ICSD no of $NiWO_4$:16685

ICSD no of $ZnWO_4$: 81937

ICSD no of α-$CoMoO_4$:23808

ICSD no of β-$CoMoO_4$:280035

ICSD no of $MgMoO_4$:20418

ICSD no of $MnMoO_4$:78328 ICSD no of $NiMoO_4$:81059

In Rietveld analysis, goodness-of-fit is important. A model is fitted to a data. If the model is correct then it will predict what the "true" intensity values should be. The most straightforward discrepancy index, the weighted profile R-factor (Rwp), follows directly from the square root of the quantity minimized, scaled by the weighted intensities:

$$Rwp^2 = \frac{\sum_i w_i (y_{C,i} - y_{O,i})^2}{\sum_i w_i (y_{O,i})^2}$$ where

wi : weight value, *yi*: intensity value, *c* is computed and *o* is observed data. Rw values should be lower than %15 to better fitting [57, 58].

The morphology of synthesized powders was also observed by scanning electron microscopy (FESEM, Nova NanoSEM 430). SEM was operated at 18 – 20 V and 3.5 – 5 spot size. For SEM analysis, powder samples were coated over the aluminium holder. If synthesized powders are not conductive, samples were coated with 10 nm gold. Although, particle size and morphologies of materials were not targeted, SEM images were taken for the determination of size and morphology of the particles.

CHAPTER 4

RESULTS AND DISCUSSION

4.1. Production Of Materials Results

12 different ABO_4 type materials (A: Cd, Co, Fe, Mg, Mn, Ni, Zn and B: W/Mo) were produced by sol-gel method to obtain powder materials. Steps and details of sol-gel method were mentioned in the experimental chapter. These materials were $CdWO_4$, $CoWO_4$, $FeWO_4$, $MgWO_4$, $MnWO_4$, $NiWO_4$, $ZnWO_4$ and $CoMoO_4$, $FeMoO_4$, $MgMoO_4$, $MnMoO_4$, $NiMoO_4$, and the results of production process of all materials were explained in this chapter below.

4.1.1. Production of $CdWO_4$

Cadmium tungstate precursor was calcinated at different temperatures (700-850 °C) for different duration (1-3 hours) to obtain desired material ($CdWO_4$). In Table 4.1, all calcination parameters which were tried to obtain $CdWO_4$ were listed.

X-Ray patterns of production of cadmium tungstate powder at 800 °C for 1 hour and 750 °C for 2 hours were shown in figure 4.1 and figure 4.2, respectively.

Table 4.1. Different calcination temperatures, duration and produced material compositions.

Temperature	Time	Composition
700 °C	1 hour	60 % $CdWO_4$-40 % WO_3
750 °C	1 hour	80% CdWO4-20 % WO_3
750 °C	2 hours	90% $CdWO_4$-10% WO_3
800 °C	1 hour	85% $CdWO_4$ - 15% WO_3
800 °C	2 hours	80% CdWO4-15 % WO_3-5 % CdO
850 °C	3 hours	80% CdWO4-10 % WO_3-10 % CdO

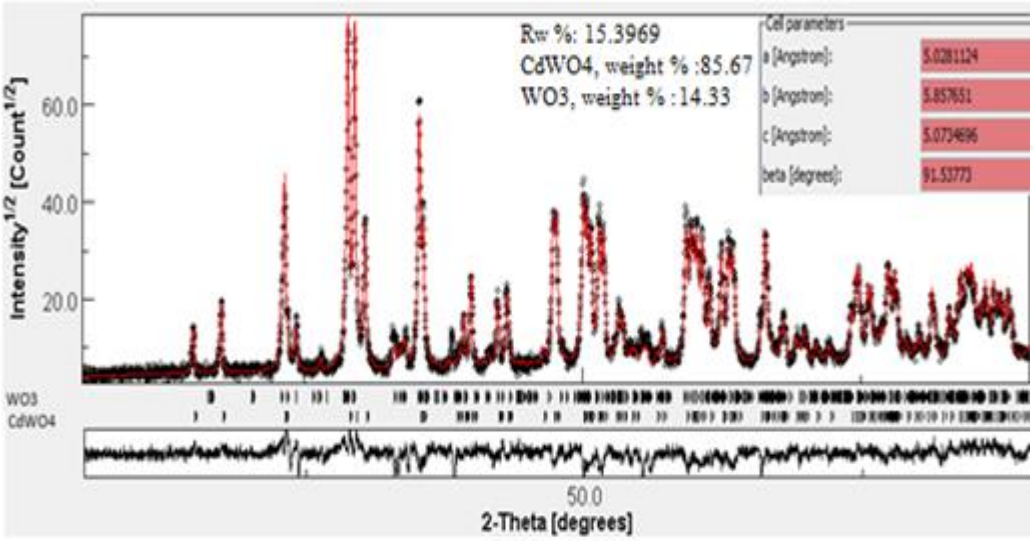


Figure 4.1. XRD pattern of $CdWO_4$ at 800 °C for 1 hour.

According to Table 4.1. and following figures, calcination temperatures and duration are important to produce desired composition. $CdWO_4$ material was produced at 750 °C / 2 hours with some impurity (WO_3).

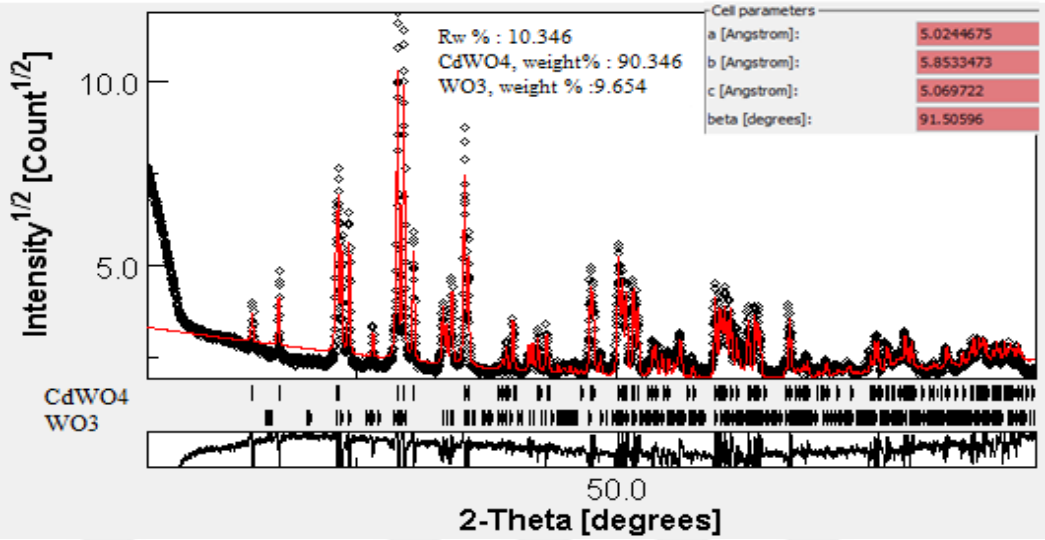


Figure 4.2. XRD pattern of $CdWO_4$ at 750 °C for 2 hours.

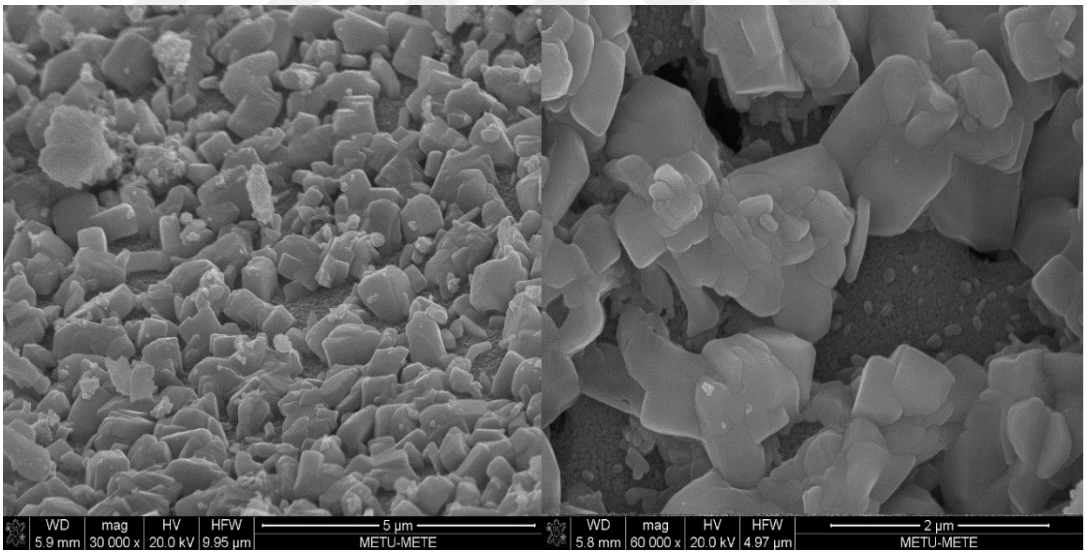


Figure 4.3. SEM images of $CdWO_4$ at 750°C for 2 hours.

SEM images of $CdWO_4$ which was produced at 750 °C for 2 hours was shown in Figure 4.3. The space group, symmetry and the lattice parameters of $CdWO_4$ and they were listed in Table 4.2. The results of refinement were same as other results in literature.

Table 4.2. Comparison of lattice parameters of $CdWO_4$.

	Symmetry	**Space group**	***a*** **(Å)**	***b*** **(Å)**	***c*** **(Å)**	***β*** **(°)**
Literature[34]	monoclinic	P2/c	5.0289	5.8596	5.0715	91.519
Experimental	monoclinic	P2/c	5.02	5.85	5.07	91.51

4.1.2. Production of $CoWO_4$

Cobalt tungstate precursor was calcinated at 800 °C for 2 hours to obtain desired material which is $CoWO_4$. X-Ray pattern of this powder was shown in Figure 4.4. According to this figure undesired phases were not observed.

SEM images after 800°C for 2 hours show various disordered, mixed morphologies. The space group, symmetry and the lattice parameters of $CoWO_4$ were listed in Table 4.3.

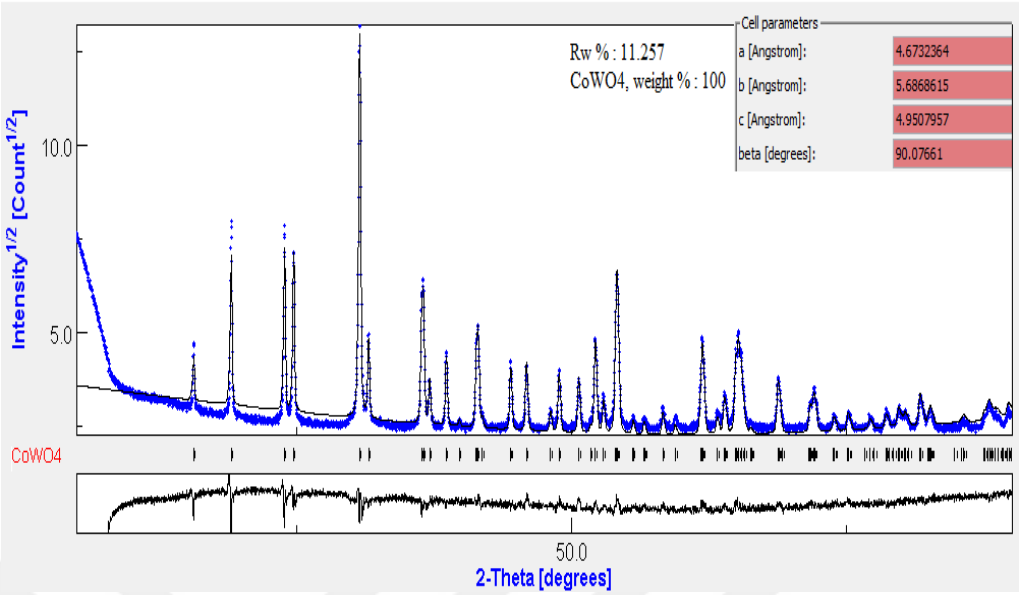


Figure 4.4. XRD pattern of $CoWO_4$ at 800 °C for 2 hours.

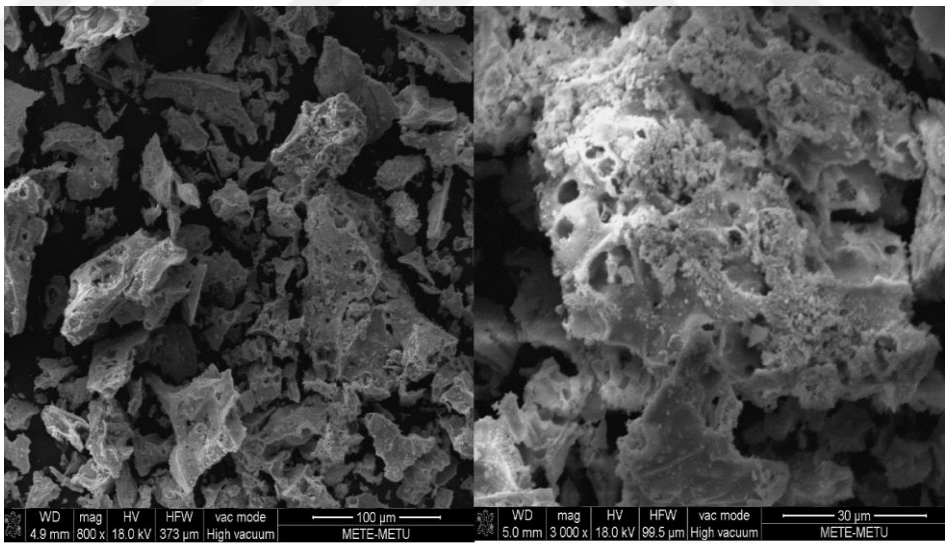


Figure 4.5. SEM images of $CoWO_4$ at 800°C for 2 hours.

Table 4.3. Comparison of lattice parameters of $CoWO_4$.

	Symmetry	**Space Group**	***a* (Å)**	***b* (Å)**	***c* (Å)**	***β* (°)**
Literature[37]	Monoclinic	P2/c	4.670	5.687	4.951	90.0
Experimental	Monoclinic	P2/c	4.67	5.69	4.95	90.08

4.1.3. Production of $FeWO_4$

In the final step of sol-gel method, precursor was calcinated 800 °C for 2 hours but $FeWO_4$ could not be produced. Then, iron source was changed from iron (III) nitrate hexahydrate to iron (II) sulphate heptahydrate, and all the steps were carried out similarly. Iron tungstate was also tried to be produced under argon atmosphere and iron (III) nitrate hexahydrate was used to be iron source. Table 4.4 shows all parameters to produce desired compound.

Argon atmosphere is tried to produce iron tungstate, because Ar is an inert gas, and if there were any reactions at air, they can be eliminated at inert (Ar) atmosphere. According to the changing of atmosphere, comparison of atmosphere also can be done.

Additionally, effect of sulphate or nitrate as an iron source can be seen. It is about the value of iron ion (Fe^{2+}) in the $FeWO_4$. In iron nitrate, oxidation state (or valence electron) of iron is (+3), however, in iron sulphate it is (+2). According to these values, synthesize of $FeWO_4$ is easy by using iron sulphate as an iron metal source.

X-Ray patterns of production of this powder at 800 °C for 2 hours for argon and air atmosphere and iron (III) nitrate hexahydrate as iron source was shown in Figure 4.6.

Table 4.4. Experimental parameters to produce $FeWO_4$.

T /time	Atmosphere	Iron source
800 °C, 2h	air	Nitrate
800 °C, 2h	air	Sulphate
800 °C, 2h	argon	Nitrate

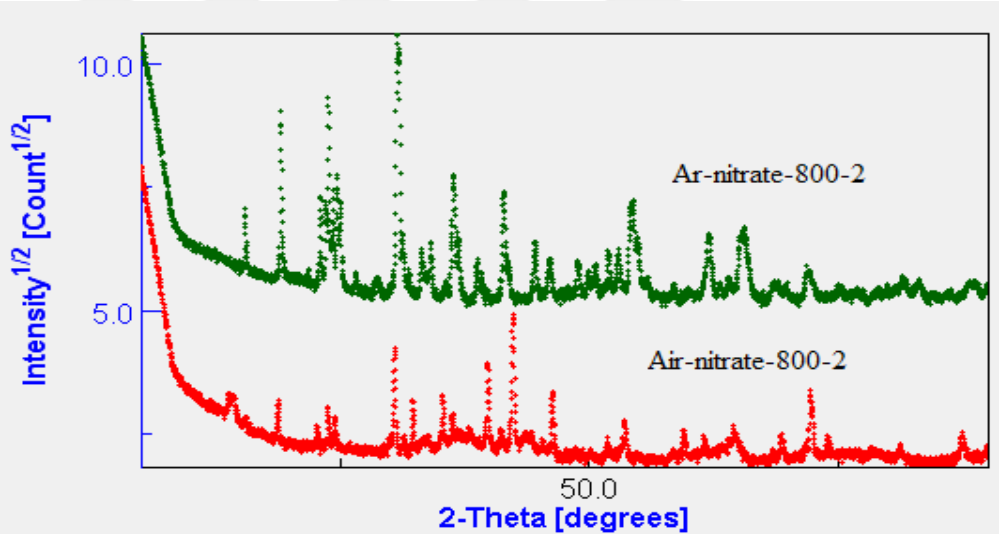


Figure 4.6. XRD patterns of $FeWO_4$ at 800 °C, 2 hours at argon atmosphere (up) and air atmosphere (bottom) and iron (III) nitrate hexahydrate as iron source.

According to Figure 4.6 changing of atmosphere was not necessary to produce iron tungstate; there were undesired peaks although all parameters were same except calcination atmosphere. However, as one can see from Figure 4.7, when iron source was changed from nitrate to sulphate and remaining parameters were not changed, desired phase which is $FeWO_4$ and some WO_3 were obtained at 800 °C, 2 hours.

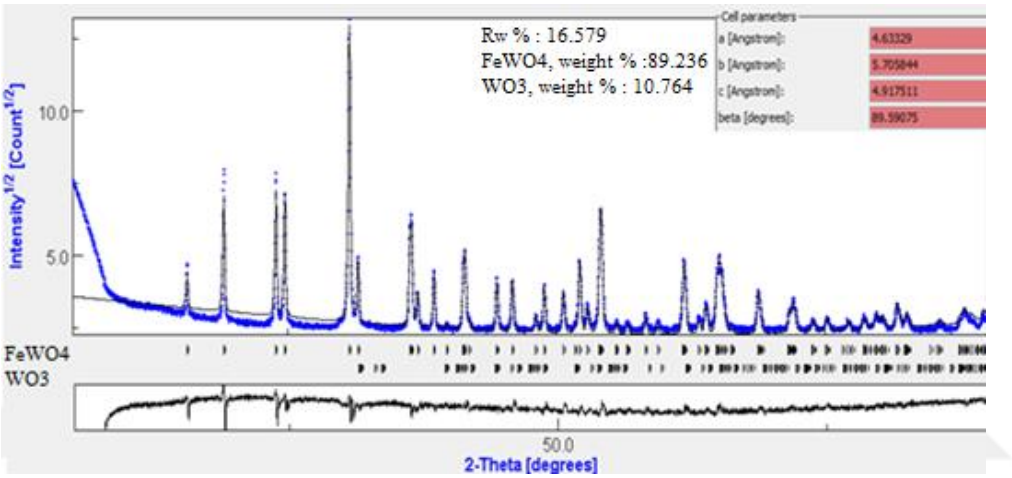


Figure 4.7. XRD pattern of $FeWO_4$ at 800 °C, 2 hours at air atmosphere, iron (II) sulphate heptahydrate as iron source.

SEM images after 800 °C for 2 hours were shown in Figure 4.8. The space group, symmetry and the lattice parameters of $FeWO_4$ were listed in Table 4.5.

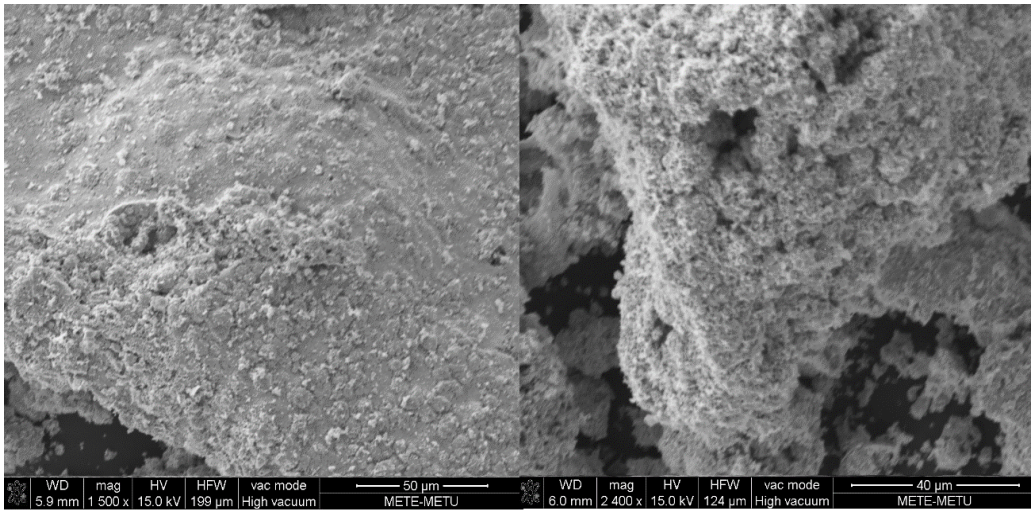


Figure 4.8. SEM images of $FeWO_4$ at 800 °C for 2 hours at air atmosphere and sulphate source.

Table 4.5. Comparison of lattice parameters of $FeWO_4$.

	Symmetry	**Space Group**	***a*** **(Å)**	***b*** **(Å)**	***c*** **(Å)**	***β*** ***(°)***
Literature[37]	Monoclinic	P2/c	4.753	5.720	4.968	90.1
Experimental	Monoclinic	P2/c	4.63	5.70	4.92	90.43

4.1.4. Production of $MgWO_4$

$MgWO_4$ precursor was calcinated 800 °C for 2 hours and desired material which is $MgWO_4$ was observed. X-Ray pattern of this powder at 800 °C for 2 hours was shown in Figure 4.9. According to this, all peaks belong to magnesium tungstate which was produced at 800 °C for 2 hours.

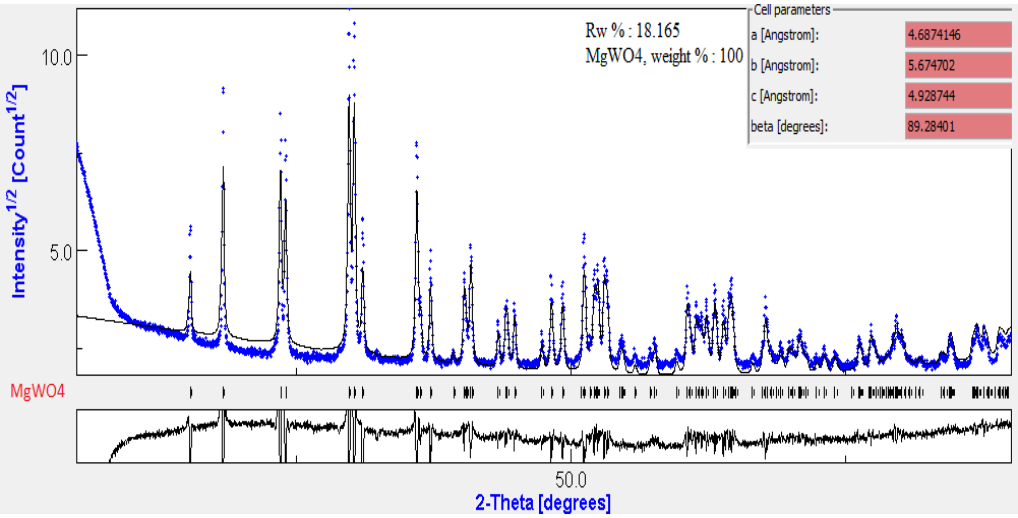


Figure 4.9. XRD pattern of $MgWO_4$ at 800 °C, 2 hours.

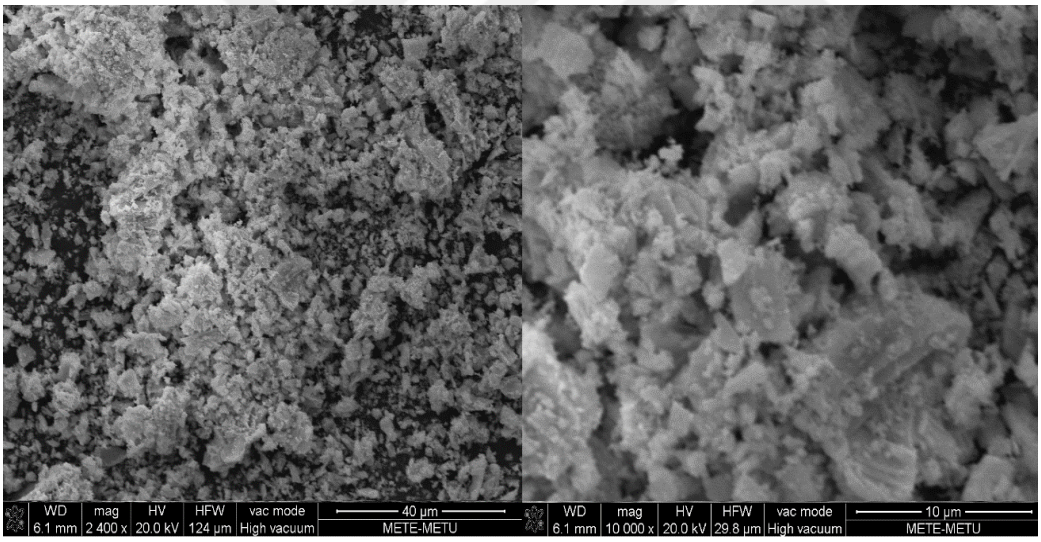


Figure 4.10. SEM images of $MgWO_4$ at 800 °C, 2 hours.

SEM images after 800 °C for 2 hours were shown in Figure 4.10. The space group, symmetry and the lattice parameters of $MgWO_4$ were listed in Table 4.6. The results of refinement were same as other results in the literature

Table 4.6. Comparison of lattice parameters of $MgWO_4$.

	Symmetry	**Space Group**	***a*** **(Å)**	***b*** **(Å)**	***c*** **(Å)**	***β*** ***(°)***
Literature[39]	monoclinic	P2/c	4.696	5.683	4.945	90.83
Experimental	monoclinic	P2/c	4.69	5.68	4.93	89.28

4.1.5. Production of $MnWO_4$

Manganese tungstate was calcinated 800 °C for 2.5 hours at the end of the sol-gel method to obtain desired material which is $MnWO_4$. X-Ray pattern of this powder at 800 °C for 2 hours was shown in Figure 4.11. According to this figure, undesired phases were not observed and all peaks belong to manganese tungstate

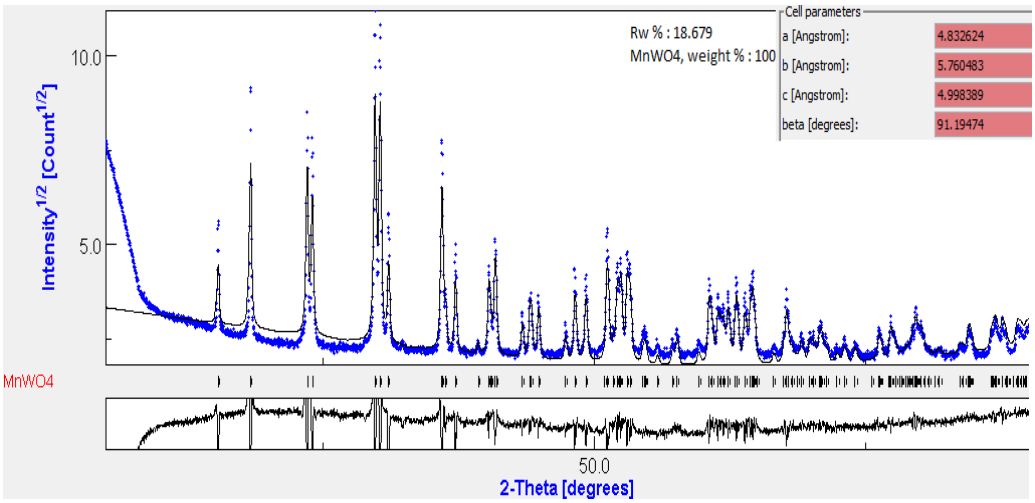


Figure 4.11. XRD pattern of $MnWO_4$ at 800 °C, 2.5 hours.

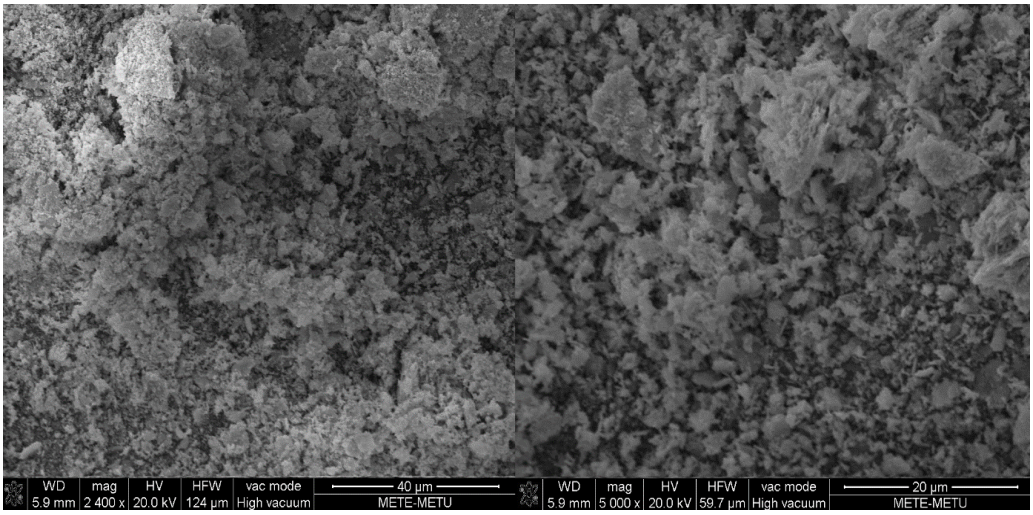


Figure 4.12. SEM images of $MnWO_4$ at 800 °C, 2.5 hours.

SEM images after 800 °C for 2.5 hours was shown in Figure 4.12. The space group, symmetry and the lattice parameters of $MgWO_4$ were listed in Table 4.7. The results of refinement were same as other results in the literature.

Table 4.7. Comparison of lattice parameters of $MnWO_4$.

	Symmetry	**Space Group**	***a*** **(Å)**	***b*** **(Å)**	***c*** **(Å)**	***β*** **(°)**
Literature[41]	monoclinic	P2/c	4.824	5.755	5.001	91.0838
Experimental	monoclinic	P2/c	4.83	5.76	4.99	91.19

4.1.6. Production of $NiWO_4$

Nickel tungstate was calcinated 800 °C for 3 hours to obtain desired material which is $NiWO_4$. X-Ray pattern of production of this powder at 800 °C for 3 hours was shown in Figure 4.13. According to this figure undesired phases were not observed.

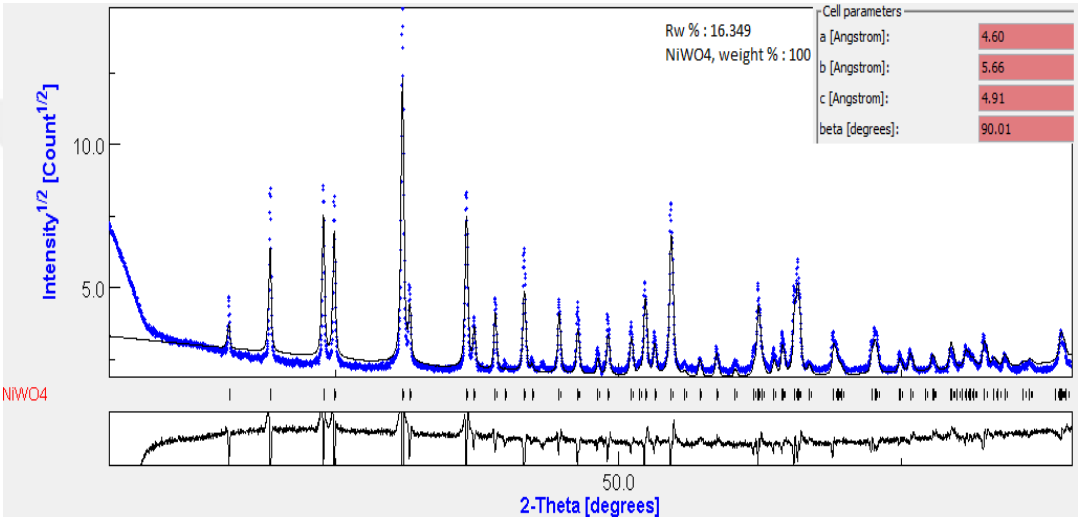


Figure 4.13. XRD pattern of $NiWO_4$ at 800 °C, 3 hours.

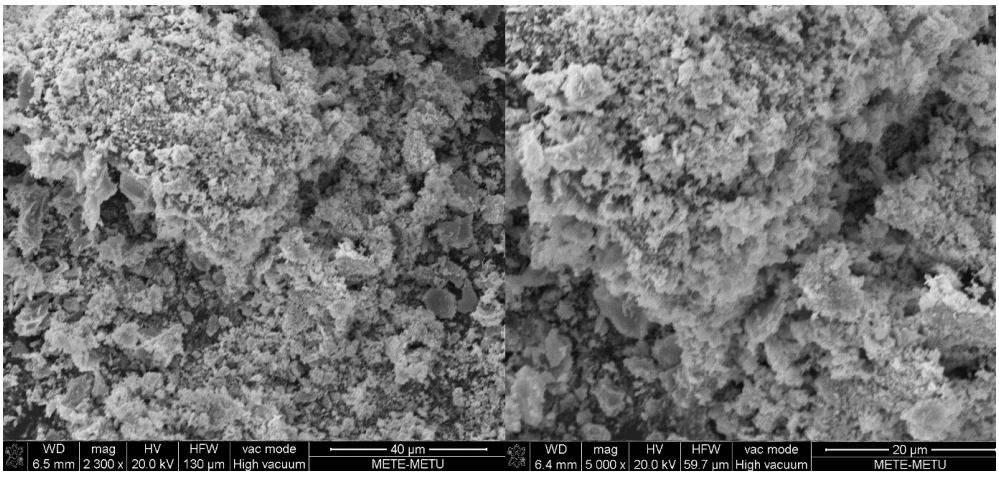


Figure 4.14. SEM images of $NiWO_4$ at 800 °C, 3 hours.

SEM micrographs after 800 °C for 2.5 hours were shown in Figure 4.14. The lattice parameters of $NiWO_4$ were listed in Table 4.8. The results of refinement were same as other results in the literature.

Table 4.8. Comparison of lattice parameters of $NiWO_4$.

	Symmetry	**Space group**	***a*** (Å)	***b*** **(**Å**)**	***c*** **(**Å)	***β*** **(**°)
Literature	monoclinic	P2/c	4.578	5.589	4.901	90.016
Experimental	monoclinic	P2/c	4.6	5.66	4.91	90.01

4.1.7. Production of $ZnWO_4$

This material was calcinated at 750 °C for 2, 4, 6 hours to obtain desired material which is $ZnWO_4$. According to following figures, calcination duration are not so important to produce desired composition at 750 °C, As a result of this section, $ZnWO_4$ material was produced at 750 °C, 2 and 4 hours showed same XRD spectrum absolutely, only intensity of last peaks in the spectrum for 6 hours were a little different. According to these results, 2 hours were enough for production of $ZnWO_4$ at 750 °C.

SEM images after 750 °C for 2 hours was shown in Figure 4.17 and micrographs showed different morphologies like as rod-like, spherical and particle size was in the micrometre range. The lattice parameters of $ZnWO_4$ were listed in Table 4.9. The results of refinement were same as other results in the literature.

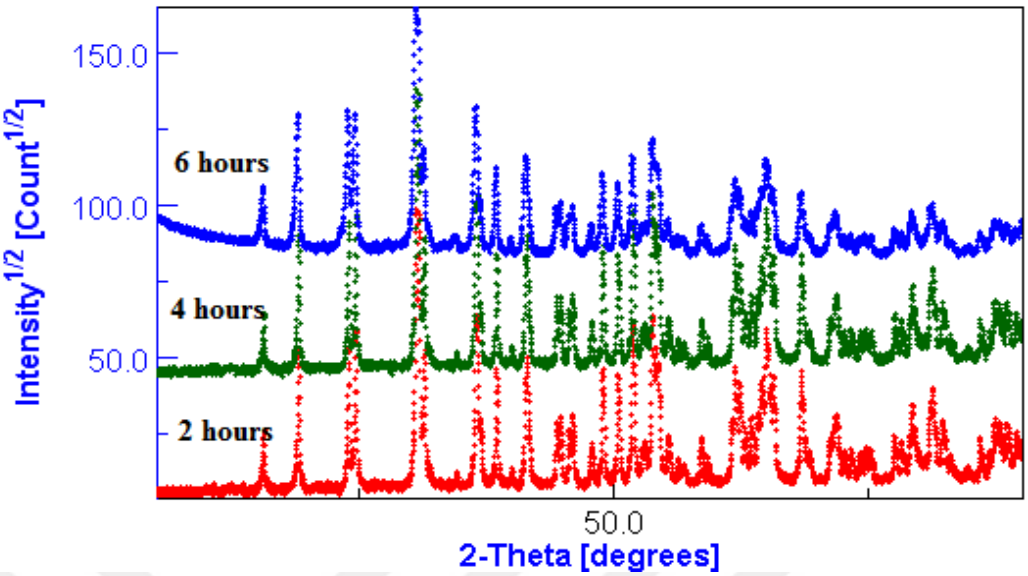


Figure 4.15. XRD spectrum for $ZnWO_4$ at 750 °C for 2, 4, 6 hours.

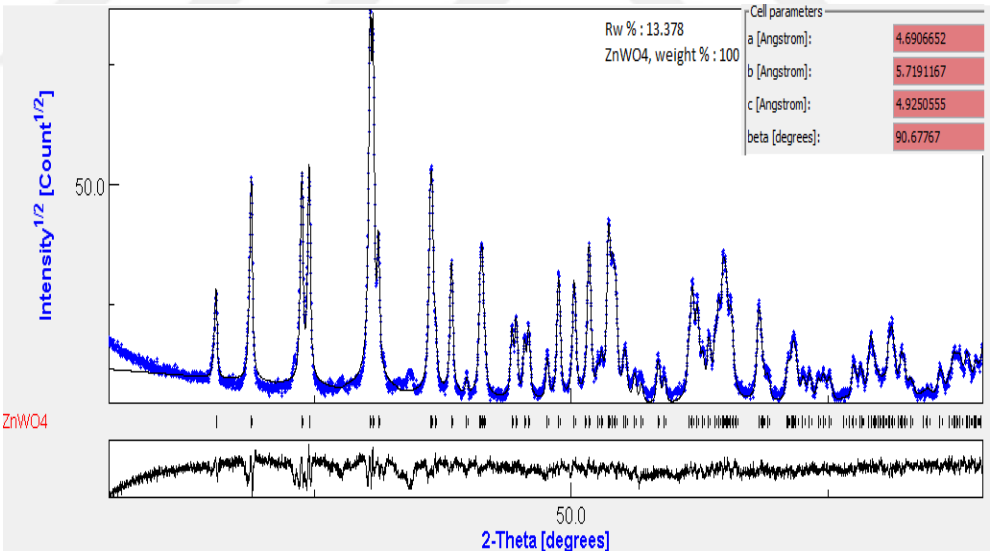


Figure 4.16. XRD pattern of $ZnWO_4$ at 750 °C, 2 hours.

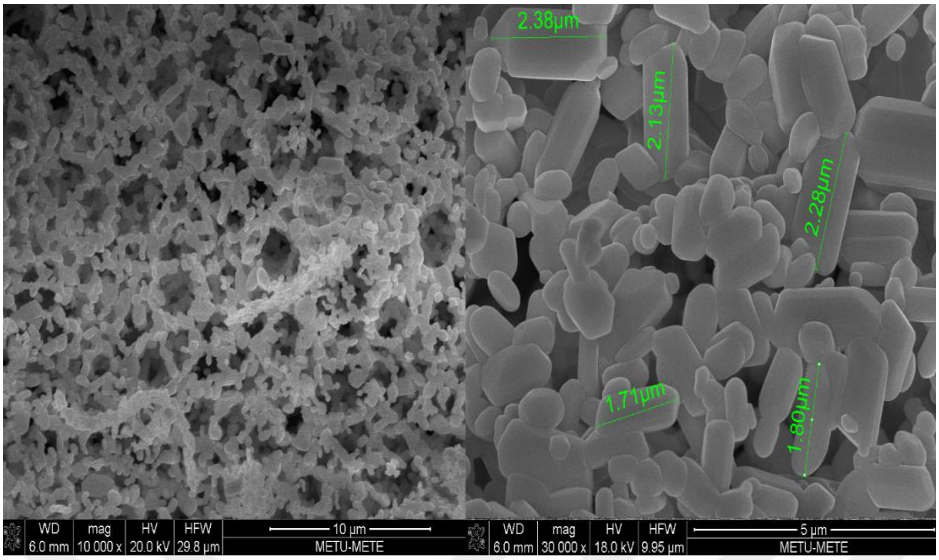


Figure 4.17. SEM images of $ZnWO_4$ at 750 °C, 2 hours

Table 4.9. Comparison of lattice parameters of $ZnWO_4$.

	Symmetry	**Space Group**	***a*** **(Å)**	***b*** **(Å)**	***c*** **(Å)**	***β*** **(°)**
Literature[46]	monoclinic	P2/c	4.690	5.716	4.927	90.626
Experimental	monoclinic	P2/c	4.69	5.72	4.93	90.68

4.1.8. Production of $CoMoO_4$

To produce cobalt molybdate powder, this precursor was calcinated 750 °C / 3h, 750 °C / 8h, 800 °/ 2h, and 850 °C / 3h to obtain desired material which is $CoMoO_4$. In the literature, $CoMoO_4$ exists in several polymorphic forms. β-$CoMoO_4$ is more stable form at low temperature. It has a monoclinic unit cell (space group C2/m) with parameters a = 9.67 Å, b = 8.85 Å, c = 7.76 Å and β = 113.88°. Above 650 K, β-$CoMoO_4$ transforms to α-$CoMoO_4$ characterized by a monoclinic unit cell (space group C2/m) and lattice parameter a = 10.21 Å, b = 9.26 Å and c = 7.02 Å and β =

106.938° [48]. Figure 4.18 showed XRD spectrum for different calcination temperatures and duration. According to this figure, there was some difference between spectrums. First difference in the spectrums is intensity difference of first two peaks. Second one is that there are very small peak after fourth peak in the spectrum of 750 °C / 8 hours and it belongs to desired phase.

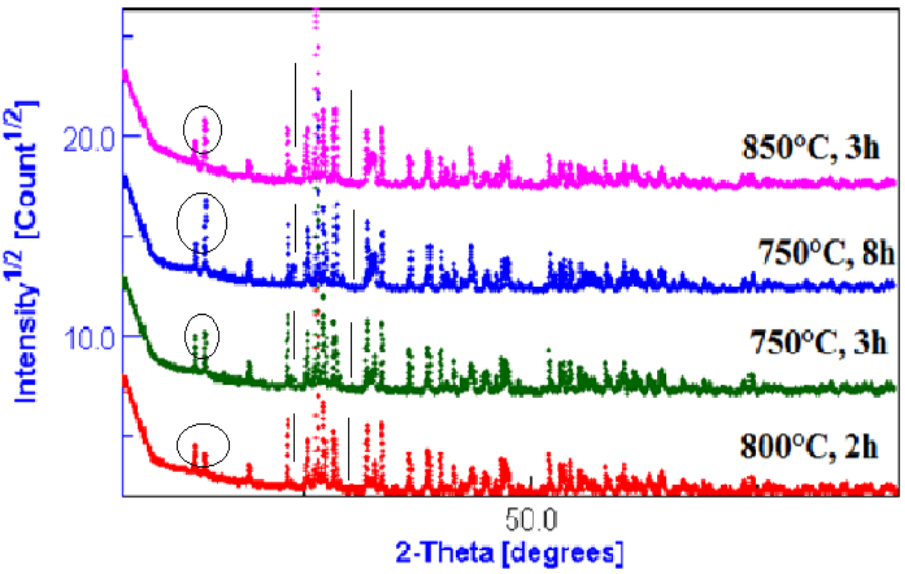


Figure 4.18. XRD spectrum of $CoMoO_4$ at different temperatures and time.

Table 4.10. Production parameters and composition of produced material.

Temperature	**time**	**Composition**	
		β-$CoMoO_4$	**α-$CoMoO_4$**
750 °C	3h	85%	15%
750 °C	8h	65%	35%
800 °C	2h	95%	5%
850 °C	3h	70%	30%

According to Table 4.10, there were different phases of cobalt molybdate, above 375 °C, 2 different cobalt molybdate phases are observed [47], preventing of formation of two phases was not possible at these temperatures and material which was produced at 750 °C, 8 hours was used for electrochemical characterization.

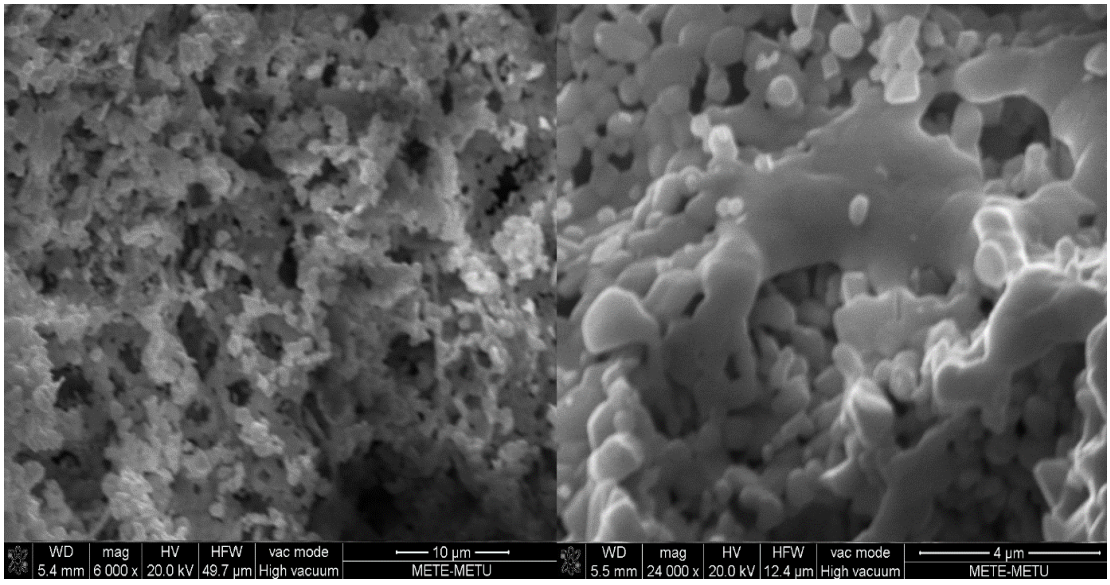


Figure 4.19. SEM images of $CoMoO_4$ at 750 °C, 8 hours.

SEM images after 750 °C for 8 hours was shown in Figure 4.19 and this micrographs showed different morphologies. The space group, symmetry and the lattice parameters of two different $CoMoO_4$ phases and they were listed in Table 4.11.

Table 4.11. Lattice parameters of different $CoMoO_4$ phases at different production parameters.

Temp.-time	**Phases**	**Symmetry**	**Space group**	***a* (Å)**	***b* (Å)**	***c* (Å)**	***β* (°)**
750 °C, 8h	*α*-$CoMoO_4$	monoclinic	C2/m	9.71	8.86	7.67	114.03
	β-$CoMoO_4$			10.25	9.29	7.04	106.92
750 °C, 3h	*α*-$CoMoO_4$	monoclinic	C2/m	9.72	8.86	7.66	114.03
	β-$CoMoO_4$			10.25	9.29	7.04	106.93
800 °C, 2h	*α*-$CoMoO_4$	monoclinic	C2/m	9.66	8.85	7.75	113.82
	β-$CoMoO_4$			10.24	9.29	7.04	106.93
850 °C, 3h	*α*-$CoMoO_4$	monoclinic	C2/m	9.71	8.86	7.66	114.06
	β-$CoMoO_4$			10.25	9.29	7.04	106.92

4.1.9. Production of $FeMoO_4$

To produce iron molybdate, powder was calcinated at 800 °C for 2 and 4 hours. According to XRD spectrum, $Fe_2(MoO_4)_3$ (orthorhombic, Pbcn space group) was produced and this material does not belongs to P2/c or C2/m space groups which were studied for this study. Because of this reason, iron molybdate were not produced again and produced ones were not used to make a cell.

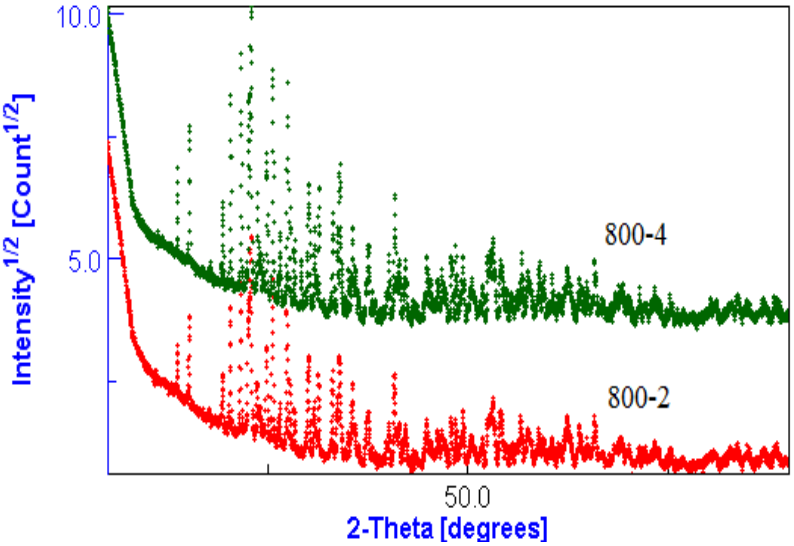


Figure 4.20. XRD spectrums of $Fe_2(MoO_4)_3$ at 800 °C 2 and 4 hours.

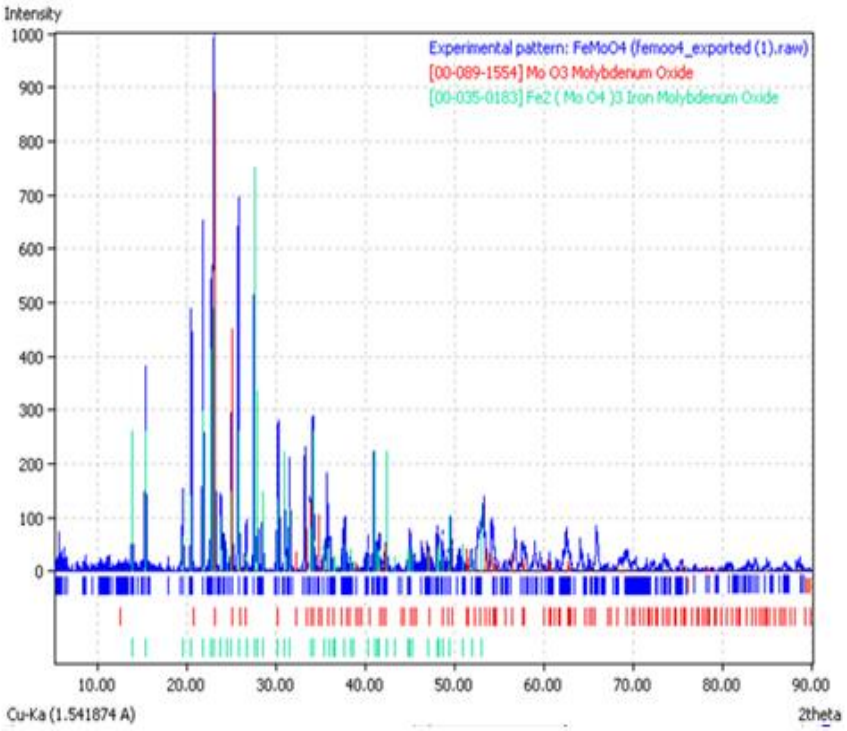


Figure 4.21. XRD spectrum of $Fe_{2\,(}MoO_4)_3$ at 800 °C 2 hours.

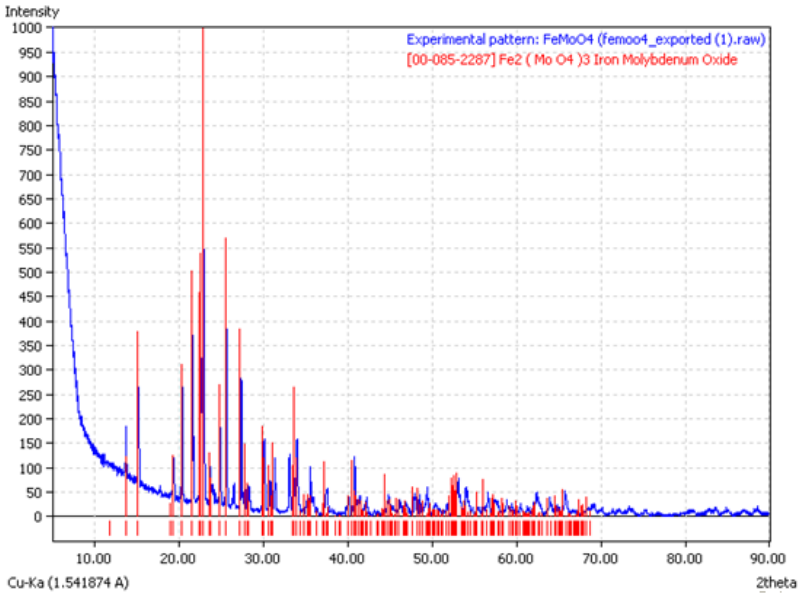


Figure 4.22. XRD spectrum of $Fe_{2\,(}MoO_4)_3$ at 800 °C 4 hours.

4.1.10. Production of $MgMoO_4$

Magnesium molybdate powder was calcinated at 750 °C for 2 and 4 hours. According to following figures, calcination durations are not so important to produce desired composition and 2 hours were enough for production of $MgMoO_4$.

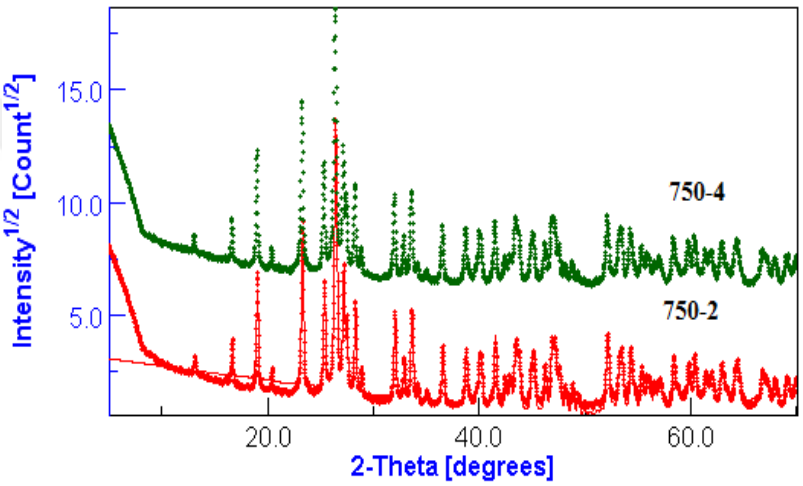


Figure 4.23. XRD spectrum of $MgMoO_4$ at 750 °C, 2 and 4 hours.

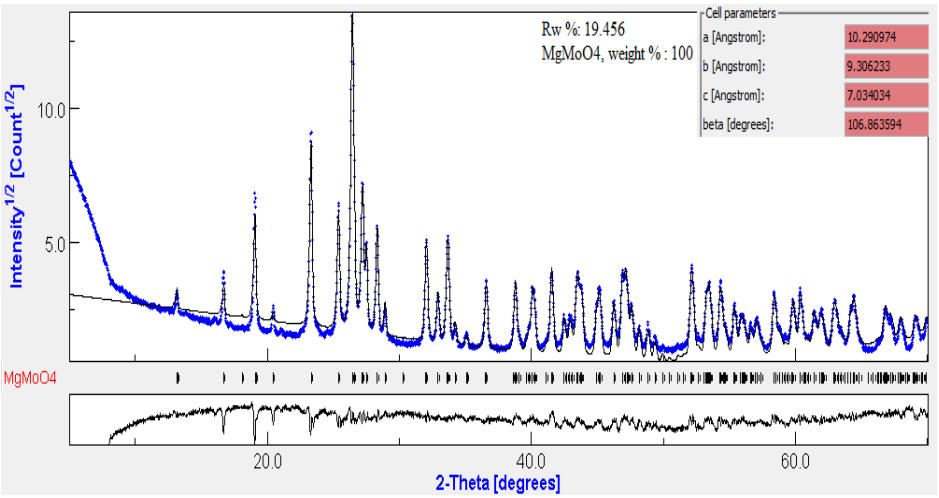


Figure 4.24. XRD pattern of $MgMoO_4$ at 750 °C, 2 hours.

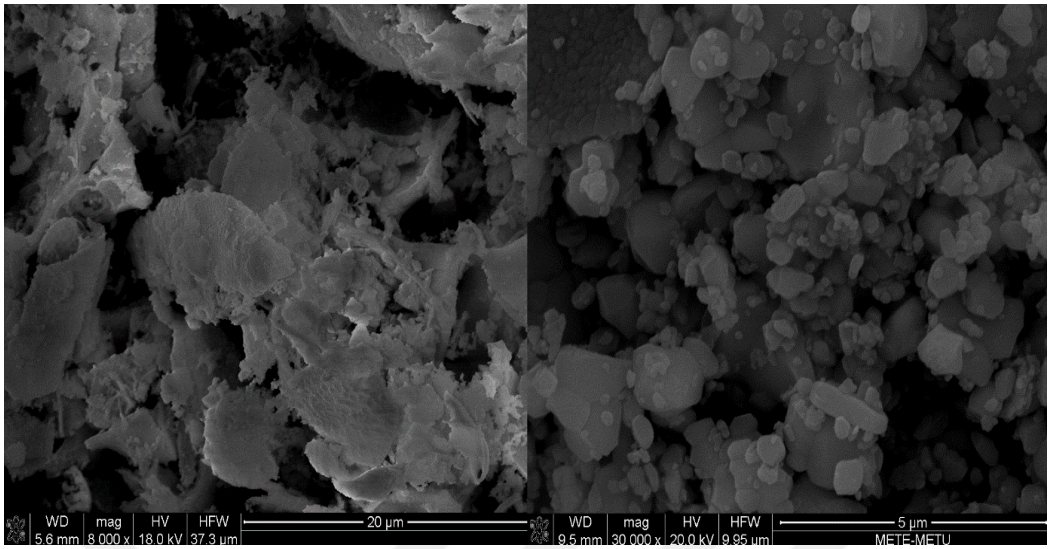


Figure 4.25. SEM images of $MgMoO_4$ at 750°C, 2 hours.

SEM images after 750 °C for 2 hours was shown in Figure 4.25. The lattice parameters of $MgMoO_4$ and they were listed in Table 4.12.

Table 4.12. Comparison of lattice parameters of $MgMoO_4$.

	Symmetry	**Space group**	***a*** **(Å)**	***b*** **(Å)**	***c*** **(Å)**	***β*** **(°)**
Literature[55]	monoclinic	C2/m	10.273	9.288	7.025	106.96
Experimental	monoclinic	C2/m	10.29	9.31	7.03	106.86

4.1.11. Production of $MnMoO_4$

$MnMoO_4$ precursor was calcinated 800 °C for 2 hours. X-Ray pattern of this powder at 800 °C for 2 hours was shown in Figure 4.26. According to this figure all peaks belong to manganese molybdate.

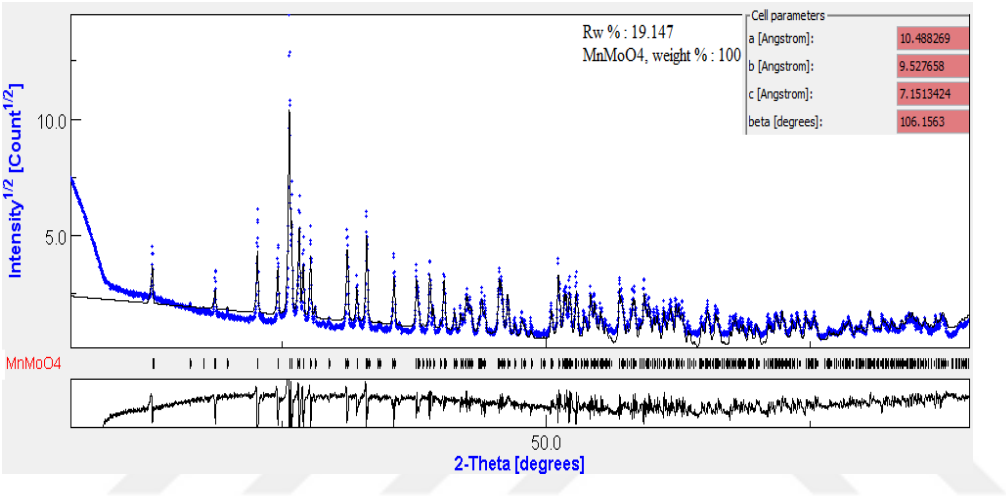


Figure 4.26. XRD patterns of $MnMoO_4$ at 800 °C, 2 hours.

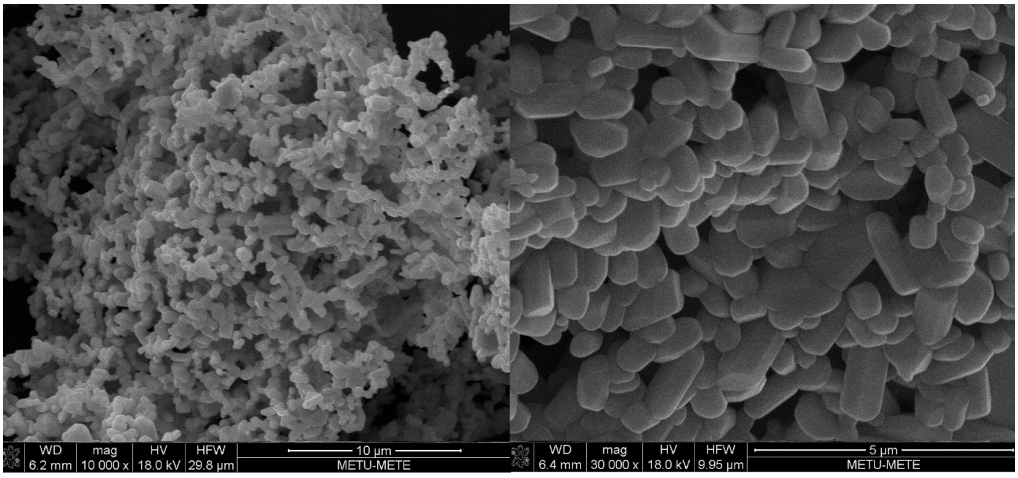


Figure 4.27. SEM images of $MnMoO_4$ at 800 °C, 2 hours.

SEM images after 800 °C for 2 hours was shown in Figure 4.27 and micrographs showed different morphologies like as rod-like, spherical and the lattice parameters of $MnMoO_4$ and they were listed in Table 4.13.

Table 4.13. Comparison of lattice parameters of $MnMoO_4$.

	Symmetry	**Space Group**	***a*** **(Å)**	***b*** **(Å)**	***c*** **(Å)**	***β*** **(°)**
Literature[57]	monoclinic	C2/m	10.499	9.530	7.151	106.2
Experimental	monoclinic	C2/m	10.5	9.54	7.16	106.15

4.1.12. Production of $NiMoO_4$

$NiMoO_4$ precursor was calcinated 800 °C for 2 hours. X-Ray patterns of nickel molybdate were shown in Figure 4.28. According to this figure undesired phases were not observed only trace amounts of nickel oxide were observed.

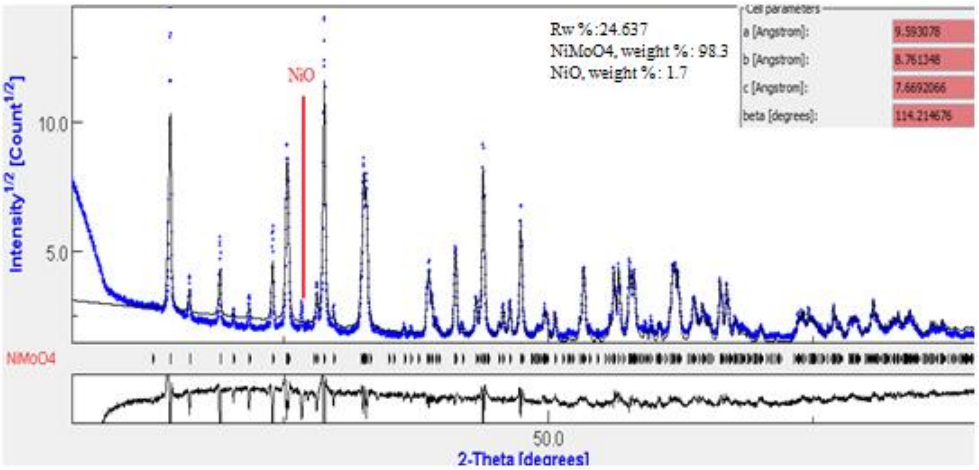


Figure 4.28. XRD pattern of $NiMoO_4$ at 800 °C, 2 hours.

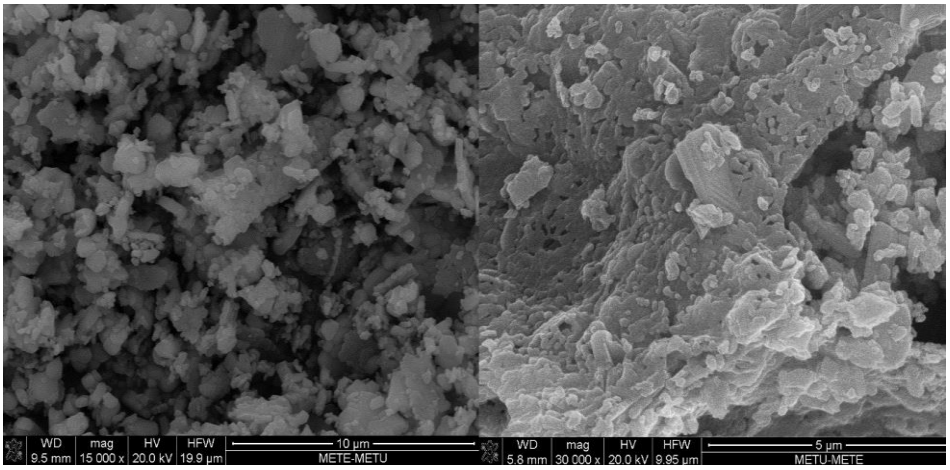


Figure 4.29. SEM images of $NiMoO_4$ at 800 °C, 2 hours.

SEM images after 800°C for 2 hours was shown in Figure 4.29 and the lattice parameters of $NiMoO_4$ and they were listed in Table 4.14.

Table 4.14. Comparison of lattice parameters of $NiMoO_4$.

	Symmetry	**space group**	***a*** **(Å)**	***b*** **(Å)**	***c*** **(Å)**	***β*** **(°)**
Literature[61]	monoclinic	C2/m	9.596	8.764Å	7.671	114.2349
Experimental	monoclinic	C2/m	9.60	8.76	7.67	114.23

4.2. Results of carbon coating of powders

Powder materials were carbon coated by mechanical milling as described in the experimental part, which were then heat treated at 650 °C for 4 h for stress relief. This was carried out under Argon atmosphere to prevent carbon oxidation. After heat treatment, XRD analysis were done again to verify the phases present, see Figure 4.30 to 4.35. As can be seen no additional XRD peaks were observed showing that

phases remain pristine. In Figure 4.36, XRD spectrum of $ZnWO_4$ was given before and after stress relieving heat treatment. It is seen that, peaks becoming broader after ball milling have slightly become narrower showing that stress relief has been somewhat achieved.

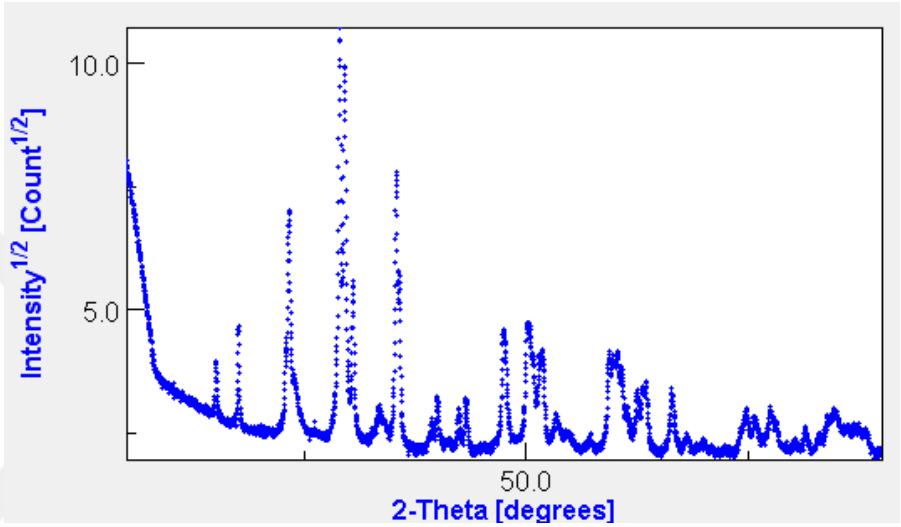


Figure 4.30. XRD pattern of carbon coated $CdWO_4$.

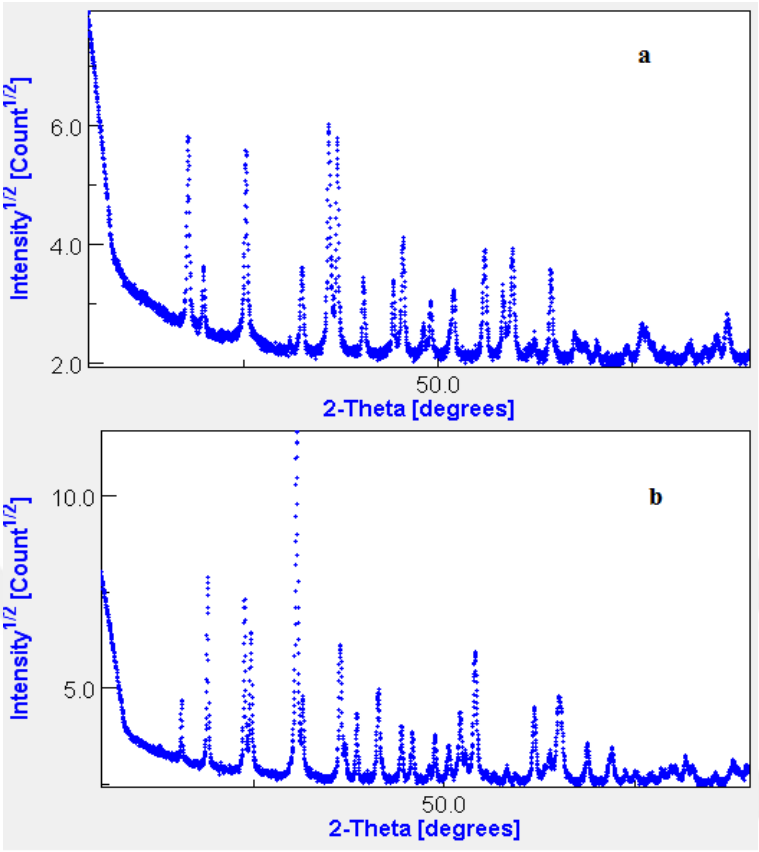


Figure 4.31. XRD patterns of carbon coated a) CoMoO4, b) CoWO4.

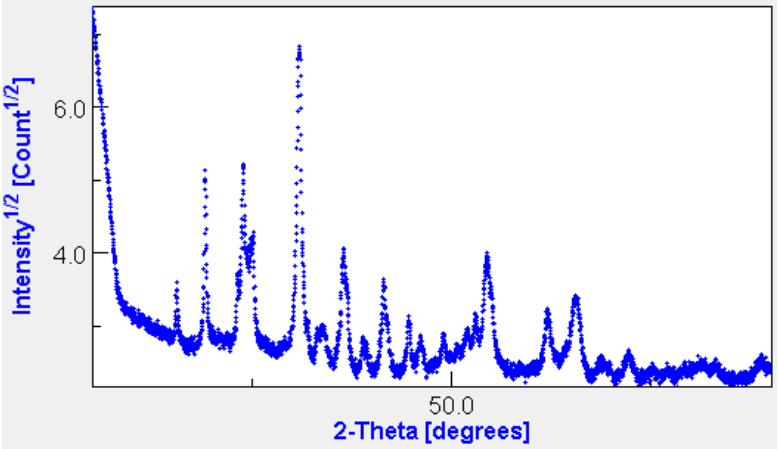


Figure 4.32. XRD pattern of carbon coated $FeWO_4$.

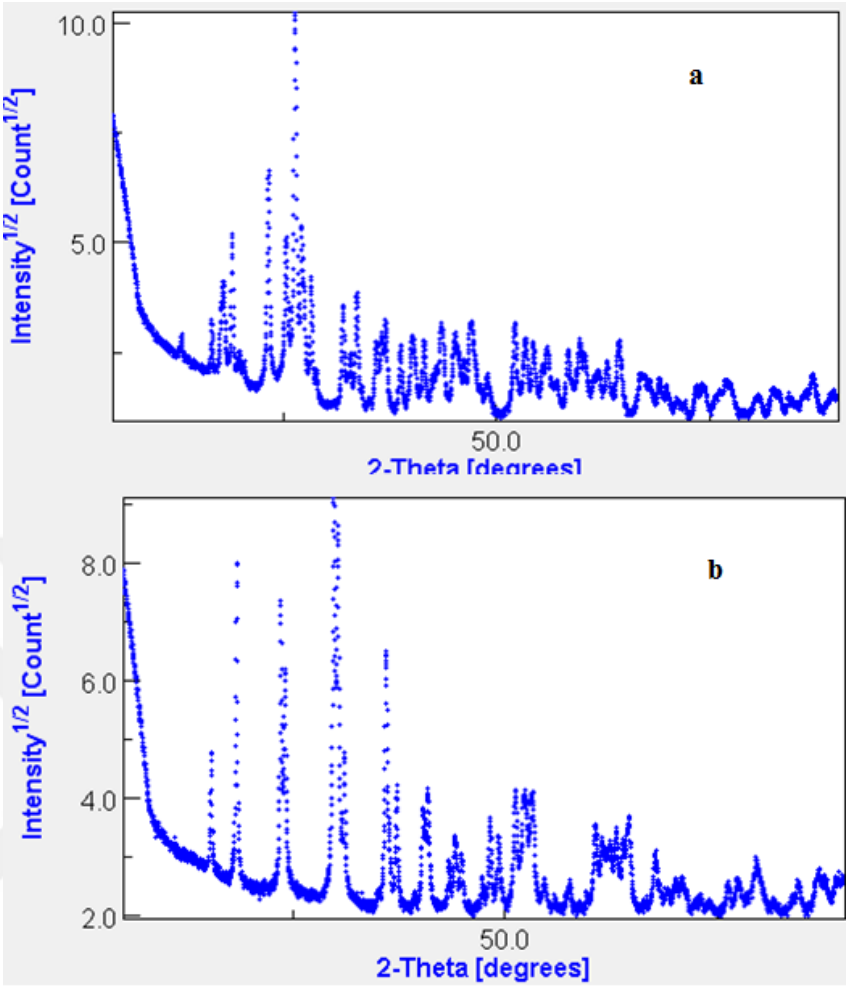


Figure 4.33. XRD patterns of carbon coated a) MgMoO4, b) MgWO4.

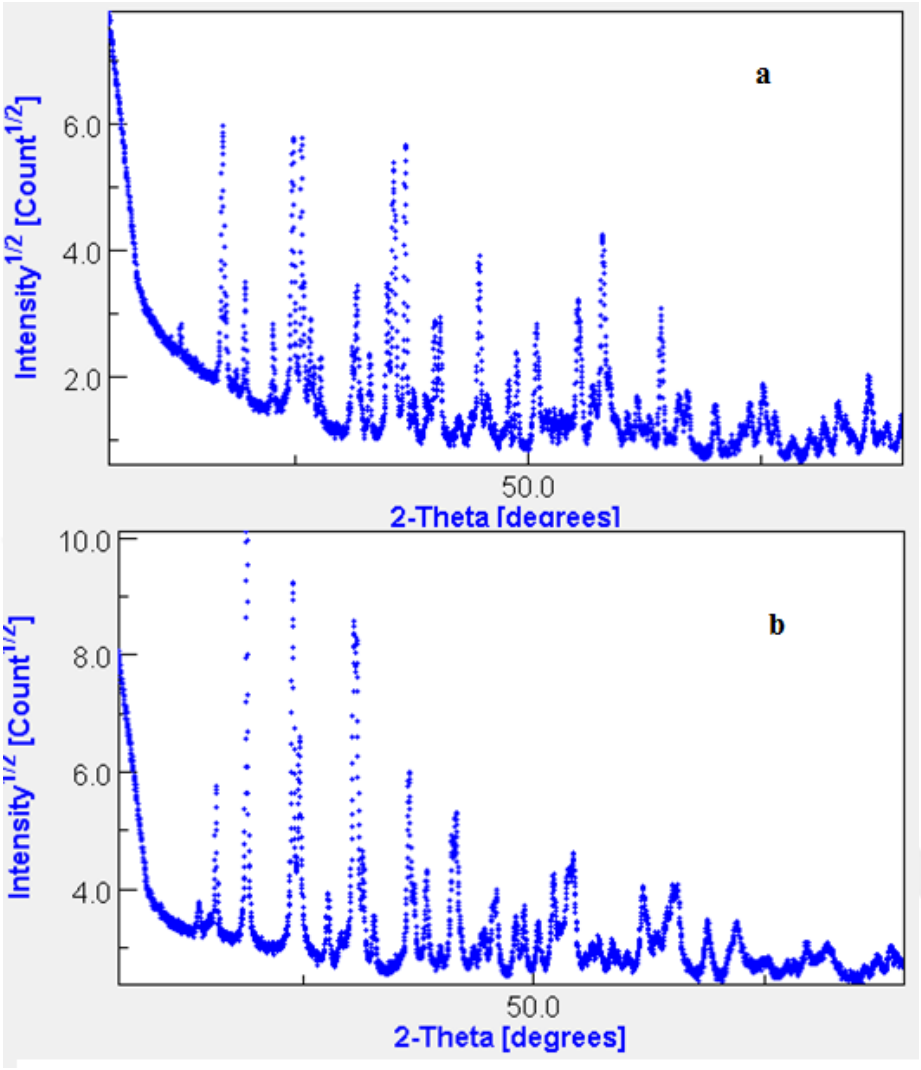


Figure 4.34. XRD patterns of carbon coated a) $MnMoO_4$, b) $MnWO_4$.

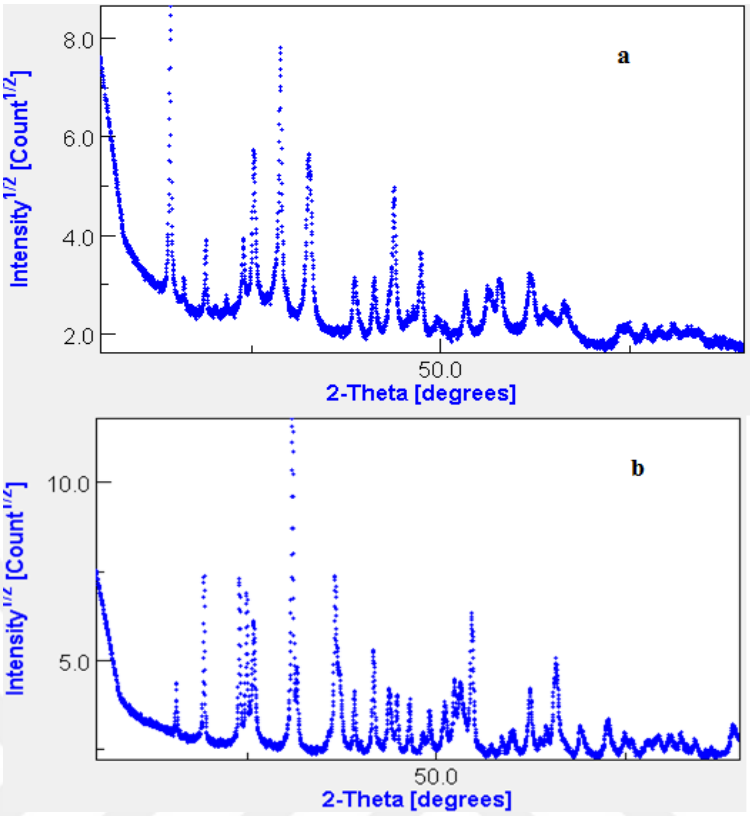


Figure 4.35. XRD patterns of carbon coated a) $NiMoO_4$, b) $NiWO_4$.

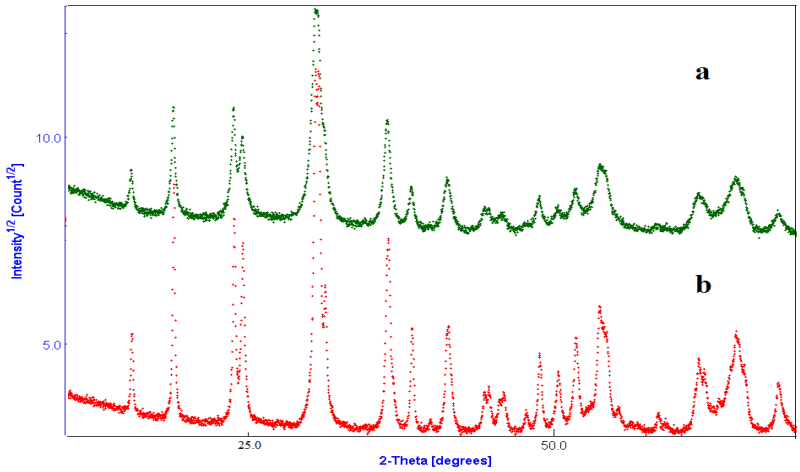


Figure 4.36. XRD patterns of carbon coated $ZnWO_4$, a) after ball mill, b) after heat treatment.

4.3. Electrochemical Tests Results

The produced active materials were electrochemically characterized after cell assembly as described before.

4.3.1. Galvanostatic Charge-Discharge tests

Synthesized active materials initially do not contain any lithium. Cells made up of these electrodes, therefore should be discharged first against metallic lithium anode to let lithium atoms insert into the active materials. This first discharge was carried out at 0.5 mA constant current and the initial discharge capacity was determined. For the continuation of the cycling, cells were charged at 0.5 mA constant current. In continuing cycles cells were again first discharged and then charged. In the next two cycles 1 mA and the following two more cycles 1.5 mA discharge/charge current was used. The cells were then finally discharged at 0.5 mA constant current. There are therefore, a total six discharge operations. The discharge capacity vs cycle number plots for molybdates and tungstates were given in Figure 4.37 and 4.38, respectively. It is seen that there is a clear decrease in the discharge capacity after the first cycle. As cycle number increases, fading of the discharge capacity continue. At the initial discharge stage of molybdates carried out at 0.5 mA constant current, manganese molybdate showed the highest capacity (1350 mAh/g) and magnesium molybdate showed the lowest one (630 mAh/g). Initial discharge capacities of tungstates, however were lower than molybdates as expected due to heavy W atom. Iron tungstate showed the highest (950 mAh/g) and magnesium tungstate showed the lowest discharge capacity (370 mAh/g). In Table 4.15 and 4.16, the retention of the capacity in the continuing cycles was given as a percentage with respect to the initial discharge capacity for molybdates and tungstates respectively. It is seen that, although $CoMoO_4$ has not got the highest initial discharge capacity, it is the one in which capacity is retained the most at the end of the highest rate discharge cycle (cycle no.5). In molybdates, $NiMoO_4$ is the one that retained the least capacity as low

as 9% at the end of the fifth cycle. However, lowering the rate of discharge in the last cycle, $NiMoO_4$ interestingly recovers the capacity up to 50%. For all other molybdates, there is no such high capacity recovery as discharge rate is decreased. In other words, rate capability of $NiMoO_4$ is not good, but it has also got low capacity decay at low rates. $MnMoO_4$ has the highest capacity (1350 mAh/g) in this study, in the literature [54] this material was high capacity anode; it showed ~1800 mAh/g capacity for the first lithiation.

In tungstates, $ZnWO_4$ has an initial retained about 45% of its initial capacity at the end of the fifth cycle and no gain or loss of capacity as the rate is lowered at the sixth cycle. It means that its rate capability and retention of its capacity is good. On the other hand, even though, initial discharge capacity of $FeWO_4$ is the highest among tungstates, its retention value is only 16% at the end of fifth cycle and was not recovered with lowering of the discharge rate. Cobalt, manganese and nickel tungstates behave similarly in a manner that, they suffer from capacity decay, but not as bad as $FeWO_4$, and at least they recover more of their capacity as rate is lowered. In the study of Montemayor [43], Co, Ni, Mn tungstates were studied as an anode material for lithium ion battery. Cobalt and nickel tungstates showed approximately 1100 mAh/g capacity and 12.5 lithium atoms inserted the structure at 400 °C. Manganese tungstate showed 1000 mAh/g capacity. In our study, capacity of cobalt tungstate is ~950 mAh/g, capacity of nickel tungstate is ~850 mAh/g and inserted lithium atoms numbers are 10.7 for Co and 9.4 for Ni at room temperature.

It is interesting to see that, both for $MgMoO_4$ and $MgWO_4$, after an initial loss of capacity about 75% and later it remains more or less constant whatever the applied discharge rate is.

Considering the experimentally obtained capacity of samples discharged down to 0.02 V, at the initial and final cycles, the number of lithium atoms inserted in the

compounds per unit formula were evaluated and given in Table 4.17 and 4.18 for molybdates and tungstates respectively.

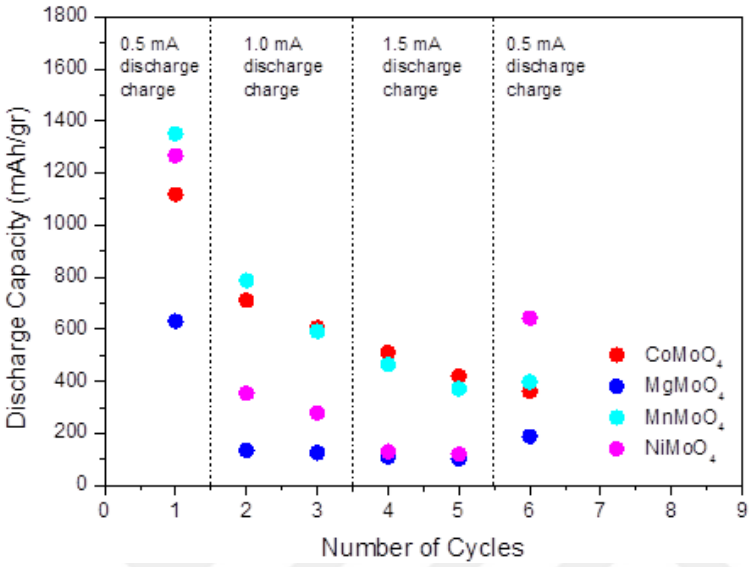


Figure 4.37. The discharge capacity graph of molybdates.

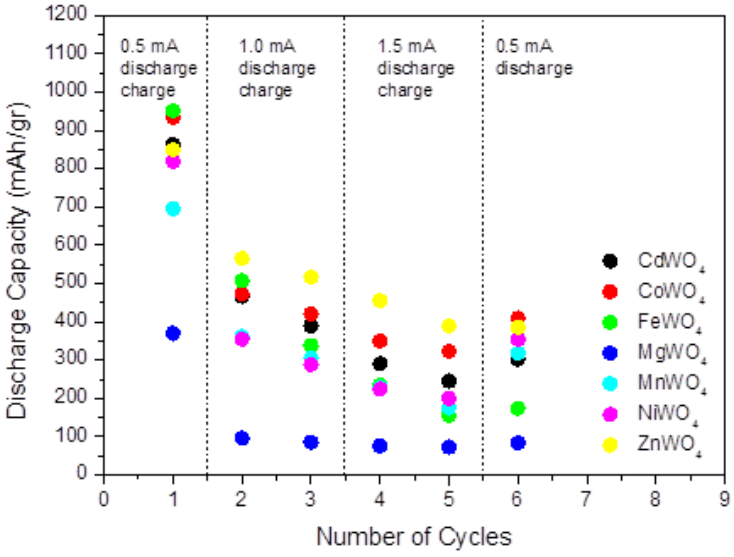


Figure 4.38. The discharge capacity graph of tungstates.

00

Table 4.15. Capacity retention of molybdates during cycling. Values were given in percentage with respect to the initial discharge capacity.

Cycle	Current (mA)	Co	Mg	Mn	Ni
2	1.0	63.6	21.5	58.3	28.0
3	1.0	54.2	20.0	43.9	22.0
4	1.5	45.8	17.4	34.4	10.3
5	1.5	37.6	16.3	27.5	9.5
6	0.5	32.4	29.9	29.5	50.7

Table 4.16. Capacity retention of tungstates during cycling. Values were given in percentage with respect to the initial discharge capacity.

Cycle	Current (mA)	Cd	Co	Fe	Mg	Mn	Ni	Zn
2	1.0	54.1	50.6	53.3	26.0	52.0	43.3	66.6
3	1.0	45.1	45.0	35.6	23.1	43.9	35.2	60.8
4	1.5	33.7	37.5	24.7	20.5	32.9	27.4	53.6
5	1.5	28.4	34.6	16.4	19.6	25.3	24.4	45.9
6	0.5	35.1	43.8	18.3	22.6	45.7	43.3	45.4

As can be seen from Table 4.15 to 4.18, the reversibility of the lithium insertion reaction is very limited since most of the lithium atoms cannot be extracted during charge. Another interesting and important feature is the fact that, almost for all compounds studied, the number of lithium atoms inserted into the crystal structure is very high, which varies from 8 to 11. Only for magnesium based molybdate and tungstate this number is 4 lithium atoms per unit formula. Considering the available

atomic positions for lithium insertion into these structures, even 4 number of atoms may be unrealistic assuming that host structure is not changed. Therefore, in order to see what structural changes have occurred after 6 cycles, all cells were disassembled at the final discharged state and the active materials were analysed by XRD. The XRD patterns of the electrodes were given in Figure 4.39 and 4.40.

Table 4.17. Number of lithium atoms inserted in molybdates at the initial, fifth and final cycles.

	Initial discharge	**5th discharge**	**Final discharge**
Co	9.1	3.4	3.0
Mg	4.3	0.7	1.3
Mn	10.8	3.0	3.2
Ni	10.3	1.0	5.2

Table 4.18. Number of lithium atoms inserted in tungstates at the initial, fifth and final cycles.

	Initial discharge	**5th discharge**	**Final discharge**
Cd	11.6	3.3	4.1
Co	10.7	3.7	4.7
Fe	10.8	1.8	2.0
Mg	3.8	0.7	0.9
Mn	7.9	2.0	3.6
Ni	9.4	2.3	4.1
Zn	9.9	4.6	4.5

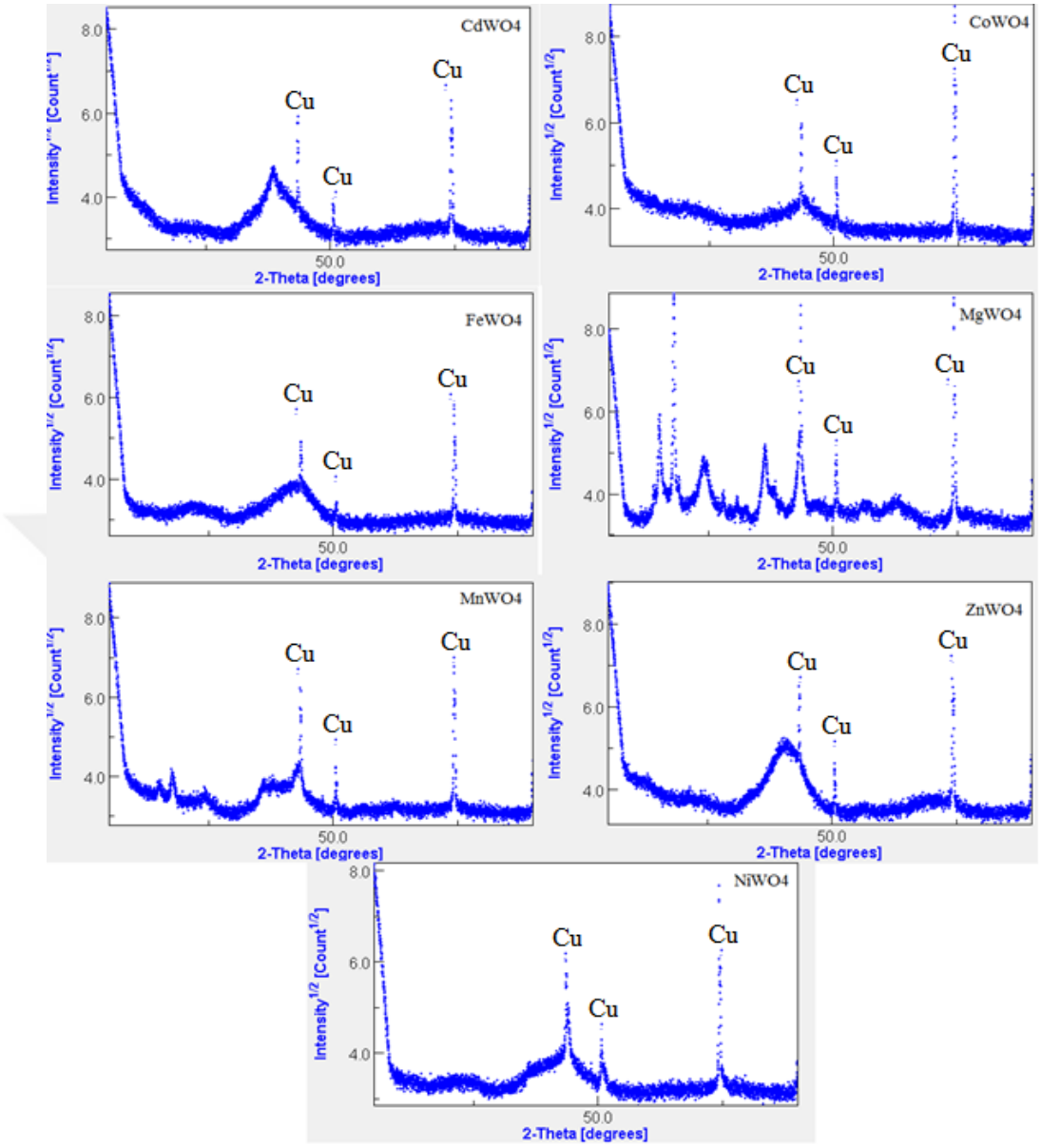


Figure 4.39. XRD spectrum of electrodes made by tungstates.

As can be seen from Figures 4.39 and 4.40, almost complete amorphization has occurred in all structures except Mg based compounds. Especially in $MgWO_4$, it is seen that crystal structure is remained within P2/c space group. Rietveld analysis shows that, lithiated structure remains in the P2/c space group with somewhat different lattice parameters due to inserted lithium atoms, see Table 4.19.

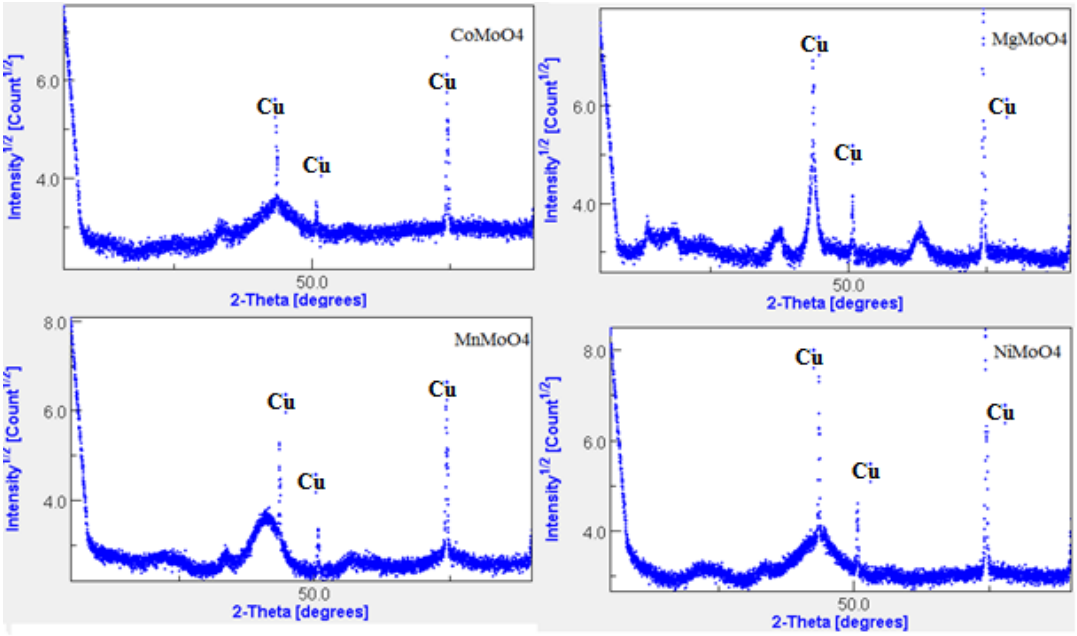


Figure 4.40. XRD spectrum of electrodes made by molybdates.

It is seen that, lithiated structure expands along *a* and *b* axis but shrinks along *c* axis, and monoclinic distortion is slightly increased. It is calculated that, volume expansion during lithiation is only 3.4 %. For $MgMoO_4$, however some crystallinity remained but definitely not within the C2/m space group. Analysing the crystal structure of $MgWO_4$, 2c (0 ½ 0) and 2d (½ 0 0) Wyckoff positions in the P2/c space group were found to be available for lithium atom occupation. These positions constitute the tunnel centre that lie along the *c* axis of the structure, see Figure 4.41. Even if both positions are filled, that makes 2 Li atoms per unit formula which is still lower than 4. It means that, 2 more lithium atoms should go to other unoccupied positions (e.g. 2a and 2b) in order not to destroy the symmetry of the P2/c group. For the other compounds where 8 to 11 lithium atoms are inserted, the structure is expected to be changed much more, because of the fact that there is no room in the structure for such large number of lithium atoms. The structure may, therefore, change so drastically that it can become amorphous. The reason why $MgWO_4$ remain crystalline may be the fact that there is so small volume change. Furthermore, uptake of more lithium atoms are not allowed probably due to strong Mg-O chemical bonds. However, upon

cycling, not all 4 atoms reversibly be extracted from the structure. In the second cycle the retained capacity is around 25% which means that 3 of 4 lithium atoms make strong bonds with oxygen atoms within the tungstate structure that remains chemically bound. In the continuing cycles, approximately one lithium atom per unit formula reversibly intercalate and deintercalate into the structure.

Table 4.19. Determined lattice parameters and unit cell volume of pristine and lithiated $MgWO_4$.

	a **(Å)**	***b*** **(Å)**	***C*** **(Å)**	***β*** **(°)**	**V** **(Å^3)**
Pristine	4.69	5.68	4.93	89.28	130.81
Lithiated	4.95	5.88	4.65	87.91	135.25

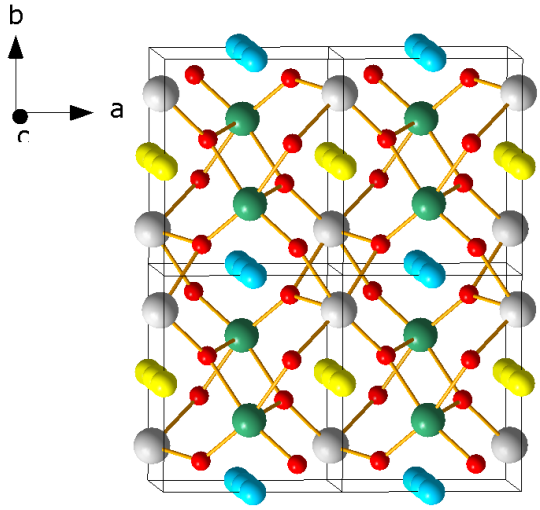


Figure 4.41. Crystal structure of $MgWO_4$, showing 2c and 2d Wyckoff positions with yellow and blue balls respectively. Grey, green and red balls represent Mg, W and O atoms respectively.

The voltage profiles of samples at the initial and final discharge operations were given in Figure 4.42 and 4.43. As seen from these figures, during the initial discharge there are several voltage plateaus at certain values. However, many of them disappear at the last discharge profile. These nearly constant potential plateaus are indicating reduction steps during the discharge process. In the study of Kim et al. [54] examining the charge discharge behaviour of $MnMoO_4$, also using measurement of XANES spectroscopy of the compound at observed plateau states, it is concluded that the plateau at 0.8 V corresponds to $Mo^{6+} \rightarrow Mo^{5+}$ reduction step. Additional plateaus they have observed at 0.6 V and 0.29 V were ascribed to $Mo^{5+} \rightarrow Mo^{4+}$ and $Mo^{4+} \rightarrow Mo^{3+}$ reduction step respectively. In our study for molybdates, voltage plateaus at around 0.8 V and 0.3 V can be clearly seen. One can also observe plateaus at 1.7 V for Ni and Co, at 1.5 V for Mn and at 1.3 V for Mg molybdate. These voltages may involve the reduction of the respective elements. At the final discharge, these plateaus almost disappear, but only in $MnMoO_4$ and $NiMoO_4$, a single plateau is observed at 0.6 V and 0.2 V respectively.

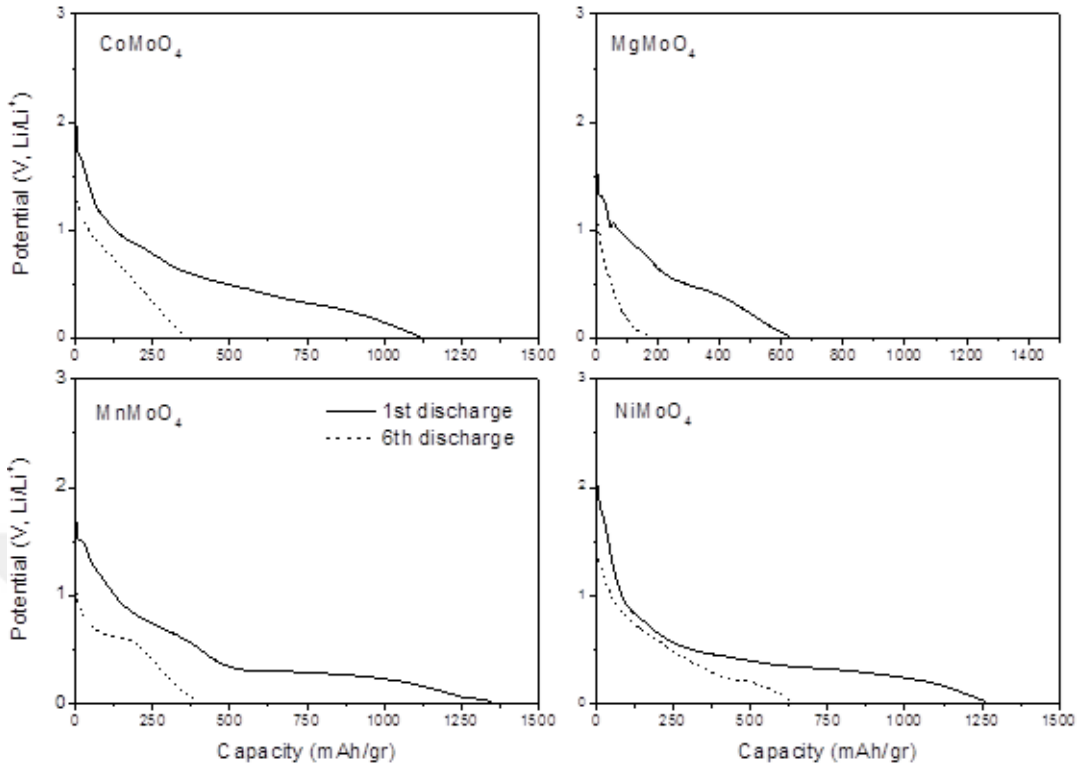


Figure 4.42. Voltage Profiles of molybdates.

During the initial discharge of tungstates, similarly, there are voltage plateaus at certain values, which then disappear completely or appear at different values. In the study of Montemayor et al. [43], examining electrochemical behaviour of $CuWO_4$, the plateau they have observed at 1.5 V was associated to $W^{6+} \rightarrow W^{5+}$ reduction step without proof. In our study, a common plateau at 0.8 V was observed for Cd, Co, Fe, Mg, Mn and Ni tungstates, which may be associated to the reduction of W from +6 to +5 valence. There seems to be another common plateau at around 0.15 V. Beyond these, there appear plateaus at higher voltages from 1.1 V to 1.5 V differing from tungstate to tungstate. ZnWO4 differs from the rest in such a way that, at the initial discharge there are plateaus at 0.6 V and 0.1 V, later at the final discharge plateau at 0.6 V disappears and another one is observed at 0.8 V.

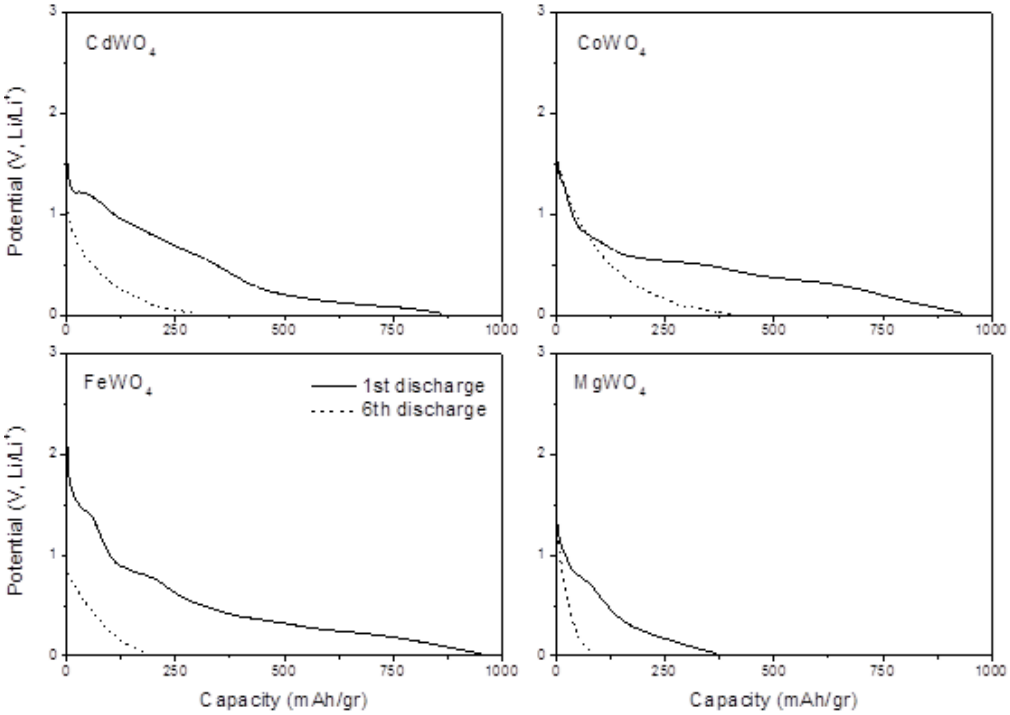


Figure 4.43. Voltage Profiles of tungstates, continued.

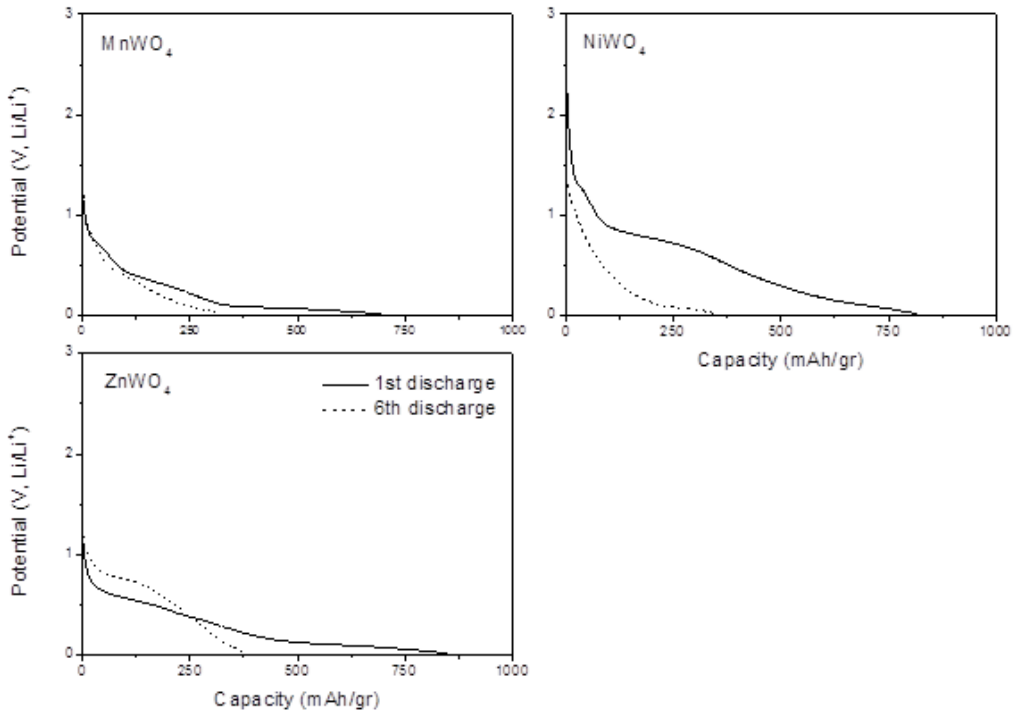


Figure 4.43. Voltage Profiles of tungstates.

4.3.2. Electrochemical Impedance Spectroscopy

The results of EIS are given in Figure 4.44. According to this figure, one can say that the cell impedance of molybdates is somewhat lower than that of tungstates. The charge transfer resistance values were determined by fitting of the EIS data to the surface film model. They were given in Table 4.20.

Table 4.20. Charge transfer resistance of molybdates and tungstates in ohm.

	Cd	Co	Fe	Mg	Mn	Ni	Zn
Molybdate	-	22.48	-	46.08	33.99	47.68	-
Tungstate	41.48	32.10	79.89	116.00	26.96	81.61	54.77

As can be seen, lowest charge transfer values were obtained in cobalt based compounds, then comes manganese based. Magnesium and nickel based compounds; on the other hand have high charge transfer resistance.

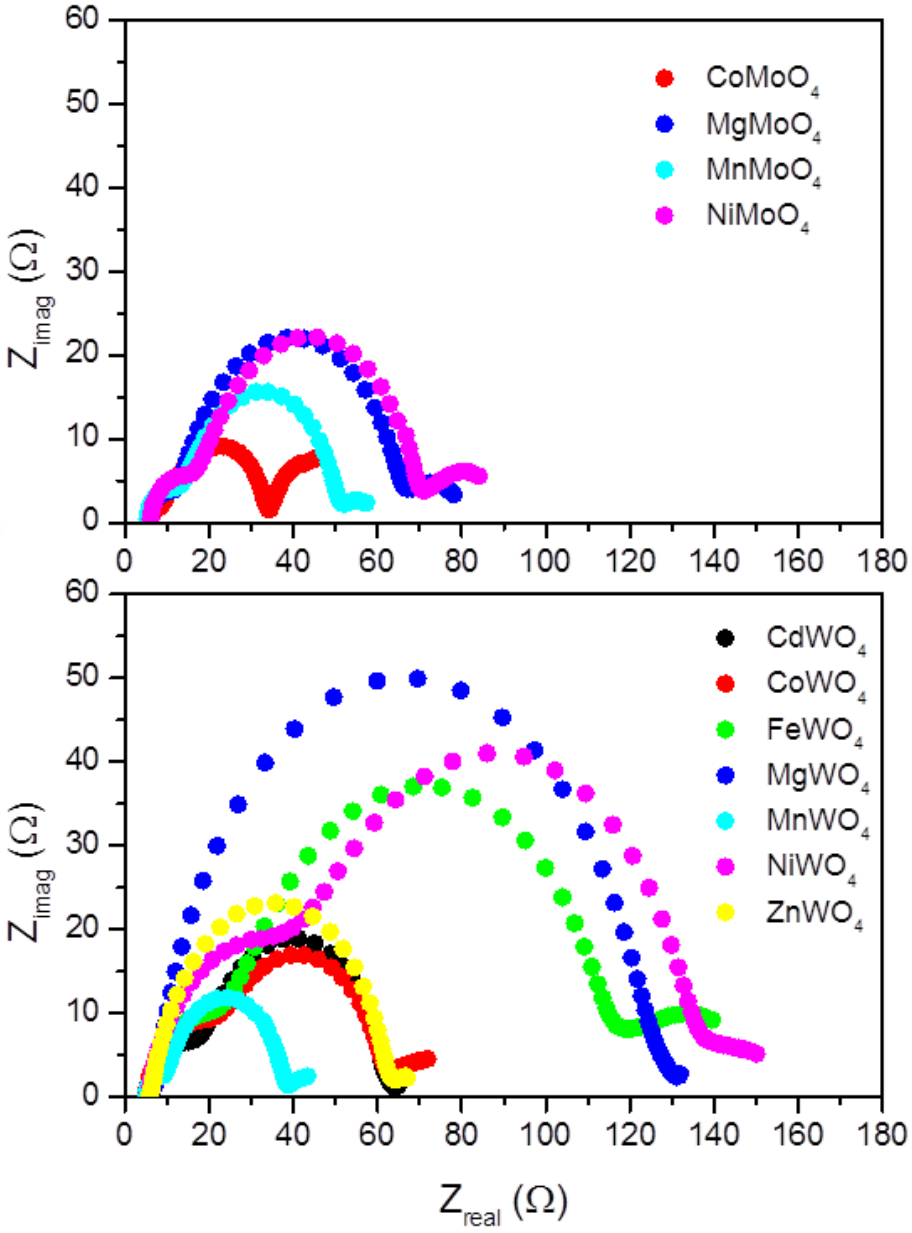


Figure 4.44. Nyquist impedance plots of materials at the discharged state.

CHAPTER 5

CONCLUSION

Metal tungstates and molybdates are important inorganic materials and they are used for so many applications, such as catalysis, magnetic applications, humidity sensors, and photoluminescence. However, their use in battery and energy storage applications are very limited. In this study, electrochemical properties of several metal molybdates and tungstates were determined for the first time. Mn, Co, Ni tungstates and Mn molybdate were studied in the literature previously. However, Cd, Zn, Mg, Fe tungstate and Mg molybdate are studied for the first time in our study.

Co, Mg, Mn and Ni molybdates and Cd, Co, Fe, Mg, Mn, Ni and Zn tungstates were synthesized using sol-gel method. All were produced by the calcination of dry gels within 750-800 °C temperature range. In $CdWO_4$ and $FeWO_4$ approximately 10 % of WO_3 appears as second phase. $FeMoO_4$ couldn't be synthesized and $NiMoO_4$ contains 1% NiO second phase.

All compounds have shown quite high capacity at the initial discharge stage. Molybdates generally have higher capacity than that of tungstates. During cycling, however, capacity decreases drastically. $MnMoO_4$ and $FeWO_4$ showed the highest capacity initially among molybdates and tungstates which are 1350 and 950 mAh/g, respectively. Their retained capacity after few cycles and rate capability, on the other hand, are not that good. Rate capability of $NiMoO_4$ is not good too. Whereas, $ZnWO_4$ has a good rate capability as well as capacity retention. Cobalt, manganese and nickel

tungstates suffer from capacity drop. It is understood that amorphization has occurred in all structures, except Mg based compounds.

According to the results of EIS, the cell impedance of molybdates was found to be lower than that of tungstates. The charge transfer resistance of the electrochemical reaction goes in the following order Co<Mn<Ni≈Mg for molybdates and Mn<Co≈Cd<Zn<Fe<Ni<Mg for tungstates.

Molybdates and tungstates in wolframite structure yield high capacity at low voltage values, which makes them a suitable anode material for lithium ion batteries. However, they suffer from capacity decay due to irreversible lithium extraction. Further research is needed to understand the lithium insertion mechanisms underlying and amorphization of the compounds.

REFERENCES

1. Reddy, T.B., *Linden's Handbook of Batteries.* 4th ed., McGraw Hill, 2010, p.1-2.

2. C. Vincent, and B. Scrosati, *Modern Batteries,* 2nd ed., Butterworth-Heinemann, 1997, p.1-17.

3. Dell, R.M., Rand, D. A. J., *Energy storage in batteries,* in *Understanding Batteries,* Royal Society of Chemistry, 2001, p.1-8.

4. Besenhard, J.O., *Thermodynamics and Mechanistics*, in *Handbook of Battery Materials*, Wiley-VCH, 2011, p. 1-26.

5. Tarascon, J.M., Armand, M., *Issues and challenges facing rechargeable lithium batteries,* Nature, Vol 414, 2001.

6. Yoshio, M., R.J. Brodd, and A. Kozawa, *Lithium-Ion Batteries Science and Technologies*, Springer-Verlag, 2009.

7. Schalkwijk, W., B. Scrosat, *Advances in Lithium-Ion Batteries*, Springer, 2002, p.1-5.

8. Mikolajczak C. et al., *Introduction to Lithium-Ion Cells and Batteries,* in Lithium Ion Batteries Hazard and Use Assessment, Fire Protection Research Foundation, 2011.

9. Tarascon, J.M., et al., *Performance of Bellcore's plastic rechargeable Li-ion batteries,* Solid State Ionics, 1996. 86–88, Part 1: p. 49-54.

10. Kayyar, A., et al., *Construction and Testing of Coin Cells of Lithium Ion*

batteries, 2012(66): p. 4104.

11. Jow, R.T. et al., *Electrolytes for Lithium and Lithium-Ion Batteries*, Springer, 2014, p.6-8.

12. Fergus, J. W., *Ceramic and polymeric solid electrolytes for lithium-ion batteries*, Journal of Power Sources 195 (2010) ,p.4554–4569.

13. Glaize, C., Geniès, S., Lithium Batteries and Other Electrochemical Storage Systems, Wiley, 2013.

14. Julien, C.M., et al., *Comparative issues of cathode materials for li-ion batteries*, Inorganics 2014, p.132-154.

15. Ohzuku, T., Makimura, Y., *Layered lithium insertion material of LiCo1/3Ni1/3Mn1/3O2 for lithium-ion batteries*, Chem. Lett. 2001, *30*, p.642–643.

16. Goodenough, J.B., et al., *Advanced electrodes for high power Li-ion batteries*, Materials 2013, 6, p.1028–1049.

17. Whittingham, M. S., *Lithium Batteries and Cathode Materials*, Chem. Rev. 2004, 104, p.4271-4301.

18. Lowe Marcy et al., *Lithium-ion Batteries for Hybrid and All-Electric Vehicles: the U.S. Value Chain*, Center on Globalization, Governance & Competitiveness Duke University,2010.

19. Nitta N., et al., *Li-ion battery materials: present and future*, Elsevier, Materials today, 2014.

20. Aifanti, K.E., *Next - Generation Anodes for Secondary Li - Ion Batteries, in High Energy Density Lithium Batteries Materials, Engineering, Applications*, Wiley-VCH, 2010.

21. Doughty, D., Rother, E.P., *A general discussion of Li-ion battery safety*, Electrochem. Soc. Interface, 2012, 2.

22. Scharner, S., et al., *Evidence of Two-Phase Formation upon Lithium Insertion into the* $Li_{1.33}Ti_{1.67}O_4$ *Spinel*, J. Electrochem. Soc., 146 (3) ,1999, p.857.

23. Wang W, et al., *Silicon-based composite anodes for Li-ion rechargeable batteries*, J Mater Chem, 2007,17, p.3229–3237.

24. Lebdeh, Y.A., Davidson, I., *Tin based anode materiald for Lithium-ion batteries,* in *Nanotecnology for lithium ion batteries*, Springer, 2013, p. 44-46

25. Wakihara, M., Yamamoto, O., *Performance of the First Lithium Ion Battery and Its Process Technology*., in *Li ion batteries fundamentals and performance*, Wiley-VCH, 1998, p.181-198.

26. Zhang, S. S., *A review on the separators of liquid electrolyte Li-ion batteries,* Journal of Power Sources, 2007, 64(1), p. 351-364.

27. Arora, P., Zhang, Z.M., *Battery separators,* Chem. Rev., 2004, 104, p.4419–62.

28. Macavei, J., Schulz, H., *The crystal structure of wolframite type tungstates at high pressure,* Zeitschrift für Kristallographie 1993, 207, p.193 – 208.

29. Ding, y, et al., *General Synthesis and Phase Control of Metal Molybdate Hydrates MMoO4 · nH2O (M) Co, Ni, Mn, n) 0, 3/4, 1) Nano/Microcrystals by a Hydrothermal Approach: Magnetic, Photocatalytic, and Electrochemical Properties,* Inorganic Chem., 2008, 47, p.7813-7823.

30. Sleight A.W., *Accurate cell dimensions for ABO_4 molybdates and tungstates,* Act Cryst, 1972, B28, p.2899.

31. Abraham, Y., et al., *Electronic structure and optical properties of $CdMoO_4$ and $CdWO_4$,* The American Physical Society, 62(3), 2000.

32. Zhang Y., Holzwarth N. A. W., and Williams R. T., *Electronic band structures of the scheelite materials $CaMoO_4$, $CaWO_4$, $PbMoO_4$, and $PbWO_4$,* Physıcal Revıew B,1998, 57, p. 12738-12479.

33. Lennstrom, K., et al., *Synthesis of $CdWO_4$ Films via Sol-Gel Processing,* Nanoscale Optics and Applications, Vol. 4809, 2002.

34**.** Shang, H.M., *Dense and optical transparent $CdWO_4$ films by sol-gel processing for scintillation applications,* J. Mater. Res., 22 (

6), 2007.

35. Rajagopal, S., *Electronic structure of $FeWO_4$ and $CoWO_4$ tungstates: First-principles FP-LAPW calculations and X-ray spectroscopy studies*, Journal of Alloys and Compounds, 496, 2010, p. 61–68.

36. Deng, J., et al., *Preparation and magnetic properties of $CoWO_4$ nanocrystals*, Cryst. Res. Technol. 47(9), 2012, p. 1004–1007.

37. Han, B., et al., *Sintering of MgO-based refractories with added WO_3,* Ceramics International, 33, 2007, p. 1563–1567.

38. Danevic, F.A., et al., *$MgWO_4$–A new crystalscintillator,* Nuclear Instruments and Methods in Physics Research A, 608, 2009, p.107–115.

39. Ye, F., et al., *Long-Range Magnetic interactions in the Multiferroic Antiferromagnet MnWO4,* Physical Review B 83, 140401(R), 2011.

40. Olabarria, U., et al., *Incommensurate magnetic structures of multiferroic $MnWO_4$ studied within the superspace formalism and A New Multiferroic Material: $MnWO_4$,* Physical Review B 87, 014419, 2013.

41. Dusastre, V., Williams, D.E., *Selectivity and composition dependence of response of wolframite-based gas sensitive resistors $(MWO_4)_x([Sn\text{-}Ti]O_2)_{(1-x)}$, $(0<x<1$, M=Mn, Fe, Co, Ni, Cu, Zn),* J. Mater. Chem. 9 (4), 1999, p. 965–971.

42. Kuzmin, A., et al., *XAS, XRD, AFM and Raman studies of nickel tungstate electrochromic thin films*, Electrochim. Acta 46 (13-14), 2001, p.2233–2236.

43. Montemayor, S. M., Fuentes, A. F., *Electrochemical characteristics of lithium insertion in several 3D metal tungstates (MWO4, M=Mn, Co, Ni and Cu) prepared by aqueous reactions*, Ceramics International 30, 2004, p.393–400.

44. Atuchin V.V., et al., *Structural and Electronic Properties of $ZnWO_4$(010) Cleaved Surface,* American Chemical Society, 11, 2011, p. 2479–2484.

45. Hung, M.N., et al., *Controlled synthesis of the $ZnWO_4$ nanostructure and study of their structural and optical properties,* Journal of Nonlinear Optical Physics & Materials, Vol. 21(1), 2012.

46. Moura, A.P., et al., *Photoluminescent Properties of $CoMoO_4$ Nanorods Quickly Synthesized and Annealed in a Domestic Microwave Oven, Advances in Chemical Engineering and Science*, 2, 2012, p. 465-473.
47. Park et al. *Electrochemical performance of $Ni_xCo_{1-x}MoO_4$ ($0 \leq x \leq 1$) nanowire anodes for lithium-ion batteries* Nanoscale Research Letters 7:35, 2012.
48. Jacob, K.T., Varamban, S.V., *Phase equilibria and thermodynamic properties of ternary oxides in the system Co–Mo–O*, Journal of Alloys and Compounds 280, 1998, p.138–146.
49. Hussain Al-Ghanem, *Evaluation of nanoparticles iron molybdate catalysts using physical properties measurements*, Wichita State University, 2006.
50. Braziulis, G., et al., *Aqueous sol–gel synthesis and thermoanalytical studyof the alkaline earth molybdate precursors*, Springer, 2013.

51. Yoon, Y.S., et al., *Structures and catalytic properties of magnesium molybdate in the oxidative dehydrogenation of alkanes $MgMoO_4$*, Catalysis Letters 59, 1999, p.165–172.
52. Li, L., et al., *Growth, Mechanical, Thermal and Spectral Properties of Cr^{3+}: $MgMoO_4$ Crystal*, Plos one, 7(1), 2012.

53. Selvan, R.K., et al., *Combustion synthesis and characterization of spherical α-$MnMoO_4$ nanoparticles*, powder technology, 2012.

54. Kim, S.S., et al., *Reaction mechanisms of $MnMoO_4$ for high capacity anode material of Li secondary battery*, Solid State Ionics 146, 2002, p. 249–256

55. Ehrenberg, H., et al., *Crystal and magnetic structure of α-$NiMoO_4$*, Journal of magnetism and magnetic materials, 150, 1995, p.371-376.
56. Material analysis using diffraction written in Java by Luca Lutterotti, version 2.68, cvs update onDate: 2016/07/26 16:22:00, CEST, 2016.
57. Brian H. Toby, *R factors in Rietveld analysis: How good is good enough*, BESSRC/XOR, Advanced Photon Source, Argonne National Laboratory, Argonne, Illinois, Powder Diffraction 21 (1), March 2006

58. http://www.ing.unitn.it/~maud/Tutorial retrieved at 20/09/2016 at 21:31.

59. Cavalcante, L.S., et al., *$ZnMoO_4$ microcrystals synthesized by the surfactant-assisted hydrothermal method: Growth process and photoluminescence properties*, Colloids and Surfaces A: Physicochem. Eng. Aspects 396, 2012, p.346– 351.